International Communications in Heat and Mass Transfer 155 (2024) 107457

Contents lists available at ScienceDirect

International Communications in Heat and Mass Transfer

journal homepage: www.elsevier.com/locate/ichmt

Experimental characterization and geometrical optimization of a commercial two-phase designed cold plate

Najmeh Fallahtafti [*], Farzaneh Hosseini, Yaser Hadad, Srikanth Rangarajan, Cong Hiep Hoang, Bahgat Sammakia

Department of Mechanical Engineering, State University of New York at Binghamton, Binghamton, NY, USA

ARTICLE INFO

Keywords:
Two-phase
Heat transfer surface area
Bubble sites
Thermal resistance
Optimization
Nucleate boiling
Chip temperature uniformity

ABSTRACT

The increasing prevalence of high-performance computing data centers necessitates the adoption of cutting-edge cooling technologies to ensure the safe and reliable operation of their powerful microprocessors. Two-phase cooling schemes are well-suited for high heat flux scenarios because of their high heat transfer coefficients and their ability to enhance chip temperature uniformity. In this study, we perform experimental characterization and deep learning driven optimization of a commercial two-phase cold plate. The initial working design of the cold plate comprises a fin height of 3mm, fin thickness of 0.1 mm, and a channel width of 0.1 mm.A dielectric coolant, Novec /HFE 7000, was impinged into microchannel fins through impinging jets. A copper block simulated an electronic chip with a surface area of $1'' \times 1''$. The experiment was conducted with three different coolant inlet temperatures of 25°C, 36°C, and 48°C with varying heat flux levels ranging from 7.5 to $73.5\ \frac{\mathrm{W}}{\mathrm{cm}^2}$. The effects of coolant inlet temperatures and flow rate on the thermo-hydraulic performance of the cold plate were explored. In two-phase flow, increasing coolant inlet temperature results in more nucleation sites and improved thermal performance consequently. Thermal resistance drops with flow rate in single-phase flow while it is not affected by flow rate in nucleate boiling region. An improvement in the design of the cold plate was carried out, with the goal of increasing the number of bubble sites and flow velocity at the root fins, by cutting the original fins and creating channels perpendicular to the original channels. Three design parameters, fin height, width of machined channels, and height of short fins preserved through machined channels, were defined. It was observed that widening the machined channels and cutting fins to some point can improve the thermal performance of the cold plate. However, removing fins excessively adversely affects the thermal performance of the cold plate because of loss of heat transfer surface area. Moreover, preserving the short fins through the machined channels decreases thermal resistance as they increase heat transfer surface area and nucleation sites. Furthermore, a deep learning-based compact model is demonstrated for the two-phase cold plate design in the specific range of geometry and flow conditions. The developed compact model is utilized to drive the single and multi-objective optimization to arrive at global optimal results.

1. Introduction

The emergence of heterogeneous integration and component miniaturization in electronic systems has led to a higher power density. Therefore, higher cooling rates per unit surface area are required to retain a compact heat sink [1,2]. Thermal stresses can induce technical problems in chips, including signal delays and power leakage. To ensure a high level of reliability while minimizing the size of the heat sink, efficient cooling technology is essential. This technology should aim to minimize temperature gradients on the chip [3]. Traditional air-cooling technologies have been substituted by liquid-cooling due to the higher heat capacity and heat transfer performance of liquids. Comprehensive research has been done on liquid single-phase cooling as a potential cooling technique for high-power electronics [4–7] Nevertheless, power densities have surpassed the heat transfer limitation of conventional liquid coolants like water, rendering single-phase operation unfeasible [8]. Furthermore, employing single-phase cooling with water has its drawbacks, which encompass a significant thermal gradient on the chip surface and the adverse repercussions of potential water leakage. Two-phase cooling systems have been considered a superior alternative to conventional liquid cooling technologies because of their two distinct

---

[*] Corresponding author.
E-mail address: nfallah1@binghamton.edu (N. Fallahtafti).

https://doi.org/10.1016/j.icheatmasstransfer.2024.107457

Nomenclature

A	Cross-sectional area of the copper block neck (m^2)
c_p	Specific heat capacity of the coolant at constant pressure $\left(\frac{J}{kg.^{\circ}C}\right)$
D	Channel network diameter (m)
h_{cf}	Height of short fins maintained on the floor of the machined channels (m) (Fig. 6)
h_f	Fin height (m) (Fig. 6)
k	Thermal conductivity of copper $\left(\frac{W}{m.^{\circ}C}\right)$
$\dot{m}$	Mass flow rate $\left(\frac{kg}{s}\right)$
ONB	Onset of nucleate boiling
p_{in}	Pressure at cold plate inlet (Pa)
p_{out}	Pressure at cold plate outlet (Pa)
$\dot{q}$	Module total power (W)
Q	Flow rate $\left(\frac{m^3}{s}\right)$
Q_{in}	Electrical input power from cartridge heaters (W)
Q_{loss}	Heat loss (W)
Q_{out}	Sensible heat picked by cold plates (W)
R_{th}	Specific thermal resistance $\left(\frac{^{\circ}C.m^2}{W}\right)$
t_b	Thickness of cold plate's base (m)
t_f	Fins thickness (m)
T_b	Average temperature of cold plate's base $(^{\circ}C)$
T_{bot}	Temperature measured by thermocouple at the bottom of the copper bock $(^{\circ}C)$
T_{in}	Coolant inlet temperature $(^{\circ}C)$
T_{out}	Coolant outlet temperature $(^{\circ}C)$
T_{top}	Temperature measured by thermocouple at the top of the copper bock $(^{\circ}C)$
w_{ch}	Micro channels width of the original cold plate (m)
w_{mc}	Machined mini channels width (m) (Fig. 6)

Greek symbols

Δx	Distance between two thermocouples located at the bottom and top of the copper block (m) (Fig. A1)

advantages from a heat transfer perspective. Firstly, latent heat is employed to dissipate more heat at lower fluid flow rates, leading to a higher heat transfer coefficient. Secondly, during two-phase cooling, the wall temperature remains steady ensuring surface temperature uniformity [9–11].

Microchannel cold plates offer the potential to achieve significantly higher heat transfer rates compared to conventional cold plates, thanks to their extensive heat transfer surface area. Flow boiling within microchannels is a commonly employed method for efficiently removing high heat flux, owing to the combination of microscale hydraulic diameter and latent heat to maximize the effectiveness of the cooling system [9,12]. Although there are few instances of commercial two-phase microchannel cooling employment, it has undergone intensive research and development over the past two decades [12–15]**.** Two heat transfer mechanisms of nucleate boiling and convective boiling contribute to two-phase flow cooling. The thermal performance strongly depends on mass flux and vapor quality when convective boiling is dominant. However, under nucleate boiling-mode, the heat flux plays an effective role to determine the heat transfer coefficient [16]. Surface tension affects cooling performance significantly when working with small hydraulic diameters like mini/microchannels. Low-tension coolants, such as HFE-7100, are widely used to analyze two-phase microchannel performance [11,12,17]. Kim and Mudawar [18] compared the thermal performance of microchannel flow boiling using three common working fluids, including DI-water, HFE-7100, and R134a. Their results show that since water surface tension is higher than other coolants, it cannot provide efficient cooling as others when the width of microchannels is small.

Extensive research has focused on how geometry changes and mass flux impact thermohydraulic efficiency and boiling in two-phase microchannel heat sinks, with in-depth analysis of parameters such as fin height, channel width, aspect ratio, cross-sectional area, and hydraulic diameter. Qu and Mudawar [10] analyzed how channel dimensions affect bubbling in two-phase cooling, developing a model that integrates mechanical and thermal factors influencing bubble dynamics. Their results demonstrated that reduced flow velocities lead to larger bubbles, shifting heat transfer from nucleate to convective boiling. Lee and Mudawar [19] examined the effects of various microchannel geometries and subcooling on pressure and thermal performance using HFE7100 coolant, managing up to 700 W/cm2 heat fluxes by lowering coolant temperature. Findings indicate that smaller hydraulic diameters enhance surface wetting and heat dissipation, although very narrow channels can lead to less favorable flow transitions, impacting thermal efficiency. Harirchian and Garimella [20–23] investigated the impact of microchannel dimensions and mass flux on heat transfer and flow patterns using FC-77. Employing flow visualization, they created a flow regime map showing nucleate boiling's prevalence in wide channels at high fluxes and how vapor confinement affects early boiling stages in narrower channels. They quantified this effect by defining nondimensional parameters and a transition criterion, providing insights into flow behavior across varying channel sizes. In another study, Markel and Kul [24,25] experimentally investigated a novel heat sink design featuring an expanding cross-section and engineered nucleation sites. They compared this innovative design with two traditional heat sinks: one with parallel microchannels and another with uniform pin fins. Through the removal of certain lateral fins and adding holes, their objective was to enhance thermal efficiency and mitigate bubble blockages. Regrettably, these modifications resulted in a roughly 22% rise in pressure drop. The effect of microchannel aspect ratio variation on heat transfer coefficient and hydraulic performance using various coolants, including DI-water and dielectric coolants, has been thoroughly investigated in the literature [26–30]. The results showed that increasing the aspect ratio improves heat transfer performance until it reaches a certain point, after which it begins to degrade. Markel et al. [31] studied the effect of heat and mass flux on thermal resistance and total pressure drop maintaining a constant aspect ratio and inlet temperature. The findings demonstrate that the heat transfer coefficient has a non-linear correlation with changes in heat flux or vapor quality, whereas it proportionally increases with the rise in mass flux. Also, the results show the total pressure drop linearly relates to heat flux. Balasubramanian et al. [32,33] suggested using a stepped fin microchannel configuration, in which the aspect ratio increases as the flow proceeds, which can stabilize the boiling heat transfer mode, and improve heat transfer consequently.

Besides microchannel geometry, surface roughness can also play a significant role in determining the flow regime and heat transfer coefficient. Bai et al. [34] compared the thermal and hydraulic performance of a two-phase microchannel with a smooth and porous surface on the bottom of channel. The use of a porous coating on the surface improves thermal performance in lower vapor quality levels due to an increase in the number of bubble nucleation sites. However, high vapor qualities cause the enhancement effect of porosity to fade. Yang et al. [35] fabricated the porous surface by nanowire integration into microchannel surface and achieved similar results. The mechanism of thermal performance escalation has been proposed as capillary-induced annular

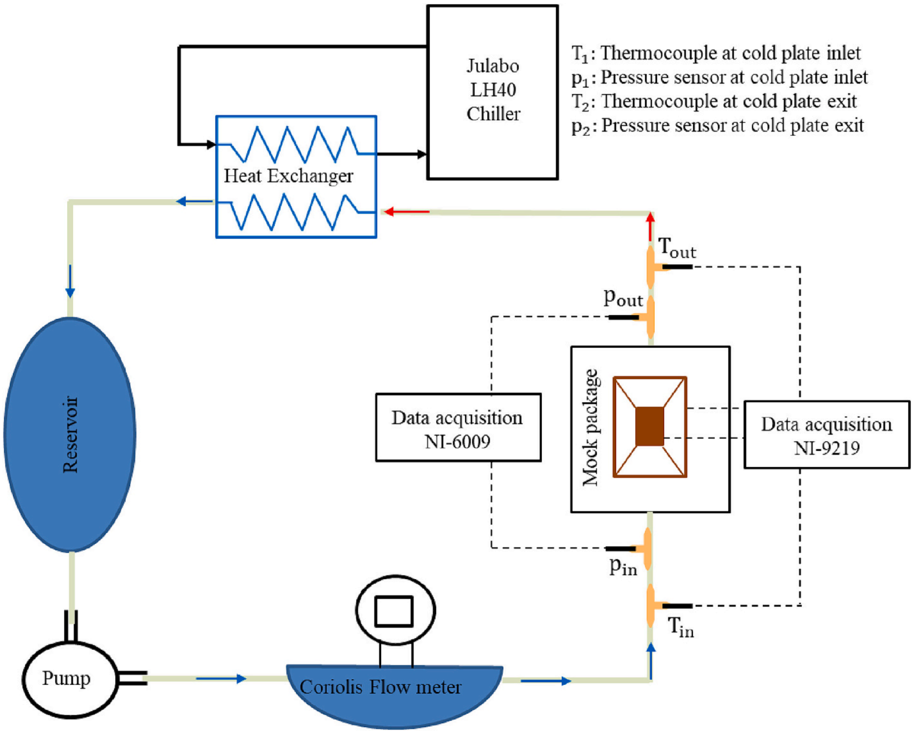

Fig. 1. Schematic of two-phase cooling apparatus.

flow. Micro pin fins at the bottom surface of each channel have been suggested as a roughening technique by Deng et al. [36]. Porous interconnected microchannel nets (PIMN) have been proposed by Chen et al. [37] as another effective approach that benefits from a combination of rough surface and the interconnected channels which relieve the channel.

Apart from the numerous experimental works reported in the literature, the numerical modeling of the two-phase flow boiling in microchannels and pin fins have gained serious attention recently. In the past, many researchers have claimed that Numerical modeling is a useful tool for better understanding the physics driving the boiling phenomena, which also allows the simulation of several scenarios where operating and geometric parameters can be readily modified. Recently a notable work from Prof. Yogendra Joshi [38,39] explored a mechanistic phase change model, which was employed with commercial computational fluid dynamics and heat transfer (CFD-HT) codes. The numerical modeling approach is validated with experimental results under various geometric and heat flux boundary conditions, making this technique an attractive alternative for designing practical two-phase micro-cooling layers operating in realistic conditions for heterogeneous integration. However, the complexity and time involved in such detailed modeling deems the numerical models less attractive and efficient, especially for a quick prediction of the performance.

In the context of Heterogeneous Integration, the correlations gain significance if they can be developed for local and global heat flux boundary conditions. Furthermore, the importance of a compact model not only lies in a quick estimation of the cold plate performance, but also it is useful in driving the optimization work. The universal correlations are sought out to be the best technique to identify the global optimal solutions among the families of cold plate. However, having a considerably accurate compact model for a particular cold plate in a given range of variables can help identify global optimal solutions for that particular cold plate. Srikanth et al. [40,41] has demonstrated compact model driven single and multi-objective optimization to identify global optimal solutions for various heat transfer problems. Balcilar et al. [42] examined the utilization of Artificial Neural Networks (ANNs) for modeling heat transfer in boiling phenomena within horizontal tubes at saturation conditions. The authors emphasize the use of ANNs to characterize traditional heat transfer surfaces and enhance predictive capability compared to conventional methods. Their study involves the development of a comprehensive neural network correlation for boiling heat transfer coefficients of specific refrigerants inside horizontal tubes using experimental data. The authors have validated their models with experimental data, noting a substantial increase in prediction capability. In addition, the authors discuss dependency analyses of inputs on the output, such as heat flux, in the artificial neural networks, along with comparisons of experimental convective heat transfer coefficients with the most predictive proposed correlation derived from optimization methods, utilizing 150 experimental data points. These findings contribute to a deeper understanding of heat transfer phenomena and the potential of ANNs in this field. Mohammadet al. [43] focused on artificial neural network modeling (ANN) of heat transfer coefficient and Nusselt number in TiO2/water nanofluid flow within a microchannel heat sink. They employ 23 and 72 datasets for the ANN modeling of heat transfer coefficient and Nusselt number, respectively. The paper outlines the ability of a well-trained network to serve as a cost-effective alternative to time-consuming experiments on nanofluid flow in microchannels. The authors demonstrate the effectiveness of artificial neural network modeling in predicting heat transfer coefficients through comparisons with experimental data. Qiu et al. [44] present an artificial neural network (ANN) model to predict the heat transfer coefficient in mini/micro-channels during saturated flow boiling. The model is based on a universal consolidated dataset that includes experimental data from various sources. Various input parameters such as mass flux, heat flux, channel diameter, and fluid properties are considered in the ANN model to predict the heat transfer coefficient. The authors conclude that the use of a universal ANN model can be an extremely useful tool for predicting heat transfer coefficients in saturated flow boiling in mini/micro-channels. Recently Mathew et al. [45] summarize the Status, Challenges, and Potential for Machine Learning in Understanding and Applying Heat Transfer Phenomena. Most studies to date have focused on developing supervised learning ML models as a replacement for empirical

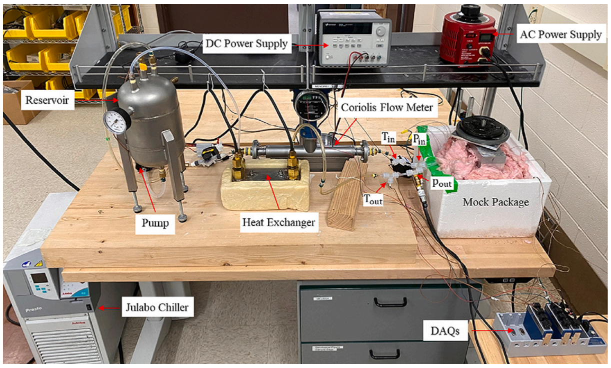

Fig. 2. Two-phase cooling apparatus.

correlations. The authors emphasize that the datasets used to train these models are large and well-distributed. While these models perform exceptionally well in interpolative scenarios, questions remain about their extrapolative predictive abilities. Mehralizadeh et al. [46] developed multiple machine learning (ML) models to forecast heat transfer coefficients for various refrigerants using different finned tubes. They concluded that the artificial neural network (ANN) outperformed the other models, achieving an exceptional R-squared value. Zhu et al. [47] constructed an ANN specifically designed to predict flow-boiling heat transfer in mini channels with serrated fins. Their model demonstrated an impressive Mean Absolute Percentage Error (MAPE). Park et al. [48] engineered neural network models to predict the channel wall temperature at Critical Heat Flux (CHF), significantly enhancing the computational speed of a thermal hydraulics simulation by up to 86% using SPACE, a specialized thermal hydraulics system code designed for nuclear reactors**.** From the literature review, it is evident that an experimental data driven optimization for a pumped two-phase cold plate is really scarce. It is also evident that ANN based deep learning is proven to improve the prediction accuracy for several flow scenarios through microchannel. Demonstration of a complete optimization by using experimental data driven compact models are necessary.

Liquid cooling including single-phase and two-phase technologies has been recognized as an efficient solution for cooling high performance electronic packages. Single-phase cooling covers a wide range of power densities. However, when working with heterogeneously integrated circuits, bringing nonuniform power maps to uniform temperature is crucial. By taking advantage of latent heat capacity and working isothermally, two-phase heat sinks have the potential to bring nonuniform power chips in quasi-uniform temperature. Design, improvement, and optimization of single-phase heat sinks has been the main subject of many studies for at least two previous decades. However, due to their modern applications and entirely different mechanism, two-phase heat sinks require special attention. To bridge the above-mentioned gap, the goal of this study is to

(1) Characterize and estimate the thermo-hydraulic performance of a commercial cold plate specifically designed for two-phase cooling in both single-phase and two-phase.
(2) Improve the cold plate performance by making changes in its architecture and adjusting it to two-phase cooling mechanism.
(3) Optimize the reformed design to reach the minimum thermal and flow resistances.

2. Experimental setup and procedures

2.1. Flow loop

A bench top apparatus as schematized in Fig.1 and shown in Fig.2 is carefully assembled to conduct experiments in a well-organized way. Starting from the reservoir, the dielectric coolant is circulated through the loop using a centrifugal pump (Make: Koolance, Part NO: PMP-600101801). The pump, controlling the flow rate of the loop, is operated by an external DC power supply (Make: Keysight, Part NO: E3634A). A flow meter (Make: Omega, Part NO: FTB 336D) with an operating range of 0.2–2 LPM is used to measure the flow rate of the liquid coolant entering the cold plate. Two thermocouples and two pressure sensors installed at the inlet and outlet of the cold plate measure coolant inlet and outlet temperature and pressure. Two T-type thermocouples are used to measure the temperature at the base of the cold plate. After departing the cold plate, the liquid-vapor mixture proceeds through a liquid-liquid heat exchanger, where the vapor is condensed, establishing the coolant temperature as re-enters the cold plate. An external chiller (Make: Julabo, Part NO: LH40) with the operating range of -40 to 250°C is used to control the temperature of the secondary loop of the condenser. Finally, the condensed coolant turns back to the reservoir. The pressure and temperature sensors are connected to data acquisition systems (DAQs) and a LabVIEW program is developed to collect the measurement data. The details of the different data sensing, their associated uncertainties and the corresponding DAQ device are listed in Table 1.

Table 1
Data sensing instruments

Instruments	Measurand	Uncertainty	DAQ Module
Pressure Gauges (Omega): PX309050A5V	P_{in}, P_{out}	±0.8 kPa	NI- USB-6009
T-type Thermocouple: Laboratory made	T_{in}, T_{out}, T_b	$\pm 0.2^{\circ}$C	NI 9219
Thermocouple (Omega): TJ36-CASS-116E-2-CC	Heat flux measurement	$\pm 0.2^{\circ}$C	NI 9219

2.2. Test section

A schematic and a picture of the mock package are shown in Fig. 3. The copper block with a cross sectional area of $1'' \times 1''$ is built to simulate a chip with uniform heat flux. The input heat of the copper block is supplied by four cartridge heaters (Make: Omega, Part NO: CIR-3020/120 V) installed in the side bottom of the copper block (Fig. 3). The cartridges are powered by an AC power supply (Make: Variac, Part NO: TDGC-2KM). Three thermocouples (Make: Omega, Part NO: TJ36-CASS-116E-2-CC) are installed along the neck of copper block to measure the temperature gradient. The heat at the top of the copper block, conducted to the cold plate, is estimated using the Fourier's law of conduction heat transfer defined by Eq. (1).

$$\dot{q} = kA\frac{\Delta T}{\Delta x} \tag{1}$$

Here, k is the thermal conductivity of copper, A is the cross-sectional area of the block neck, ΔT is the temperature difference along the copper block, and Δx is distance between two thermocouples. The cold plate is affixed on top of the copper blocks by employing a layer of thermal interface material (TIM) featuring a thermal conductivity of 12.8 $\frac{W}{m.K}$. The cold plate is then fastened in place atop the copper block with a dedicated holder. Weights sit on the weight seat to exert pressure and maintain a consistent interfacial thickness. To minimize heat loss from the copper block, it is placed on top of an insulating ceramic block (Sheffield Pottery-Model TCHTB with thermal conductivity of 0.09 $\frac{W}{m.K}$ and stable properties up to 1260 °C). The sides of the copper block are thoroughly insulated by insulation layers of fiber glass. A polystyrene box is used to contain the copper block with associated insulation and ceramic block. The levelness and the flatness of the heater surface are ensured throughout all experiments by using a level and a flatness indicator.

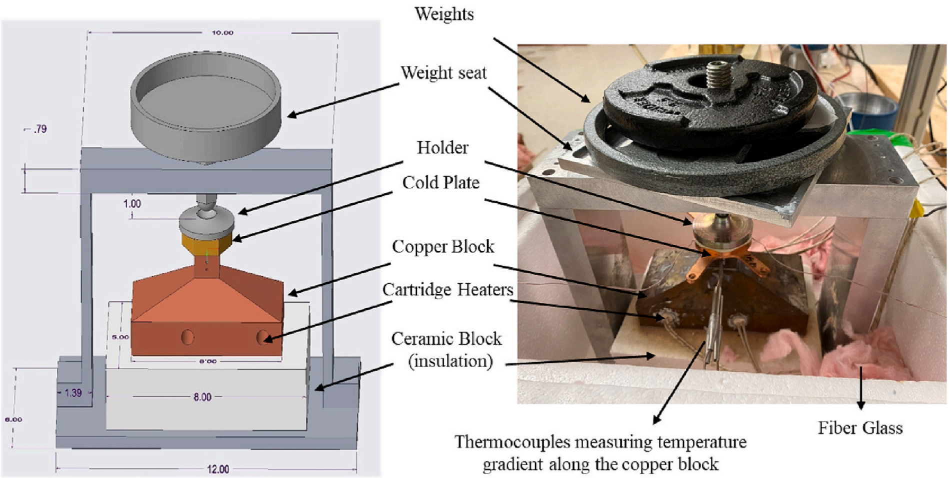

Fig. 3. Schematic and picture of the mock package.

Assembled cold plate

Cap

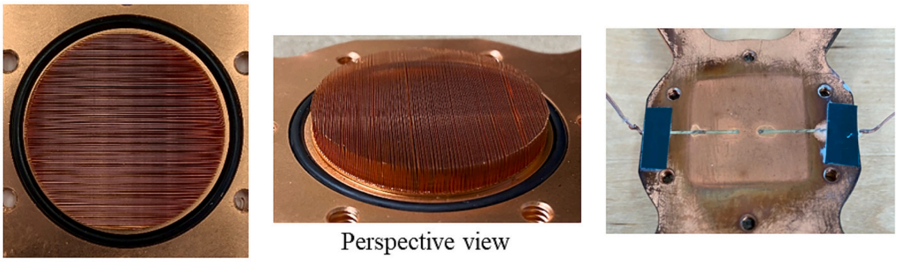

Top view

Perspective view

Thermocouples at the base
of the cold plate

Original Microchannels

Fig. 4. Cold plate fin network and manifold architecture.

2.3. *Cold plate design and fabrication*

The fin network of the original commercial cold plate (Ebullient Direct Jet Module) is shown in Fig. 4. The cold plate has been specifically designed to facilitate two-phase flow, featuring a configuration of 34 circular nozzles (jets) with a diameter of 1 mm in the cap. The 3D printed plastic cap incorporates both inlet and outlet manifolds. The coolant follows a specific path throughout the cold plate as depicted in Fig. 5. It enters through path 1–2 and then impinges down into the microchannels via the jets in path 2–3. As it travels through the microchannels in path 3–4, the coolant absorbs heat from the fin network. It proceeds toward the exit in path 4–5, and finally leaves the cold plate through path5–6. The impingement jet array is supposed to enhance chip temperature uniformity and improve convection heat transfer coefficients, benefiting both single-phase and two-phase cooling systems [49]. The cold plate's channel network is manufactured using a skiving process with initial specifications for fin height (h_f), fin thickness (t_f), and channel width (w_{ch}), set at 3 mm, 0.1 mm, and 0.1 mm respectively. There is a 0.3 mm gap between the fin tips and the lid is 0.3 mm. The channel network, as depicted in Fig. 4, exhibits a circular projected area with a diameter of 26 mm, denoted as 'D' in Table 2. The thickness of the cold plate base (t_b) is 3 mm. The original design's geometrical dimensions are listed in Table 2. In the study conducted by Hoang et al. [50] the effect of fin height on the performance of the Ebullient cold plate was explored. The finding revealed a parabolic relationship between thermal resistance and fin height. Shortening the fin height led to a decrease in thermal resistance to a certain extent. However, it should be noted that excessive fin height reduction had a detrimental impact on the cold plate thermal performance. Hoang et al. [51] conducted an additional investigation, exploring three distinct configurations for Ebullient cold plate: microchannels, pin fin arrays, and bare copper surface. Their findings indicated that the thermal performance of the

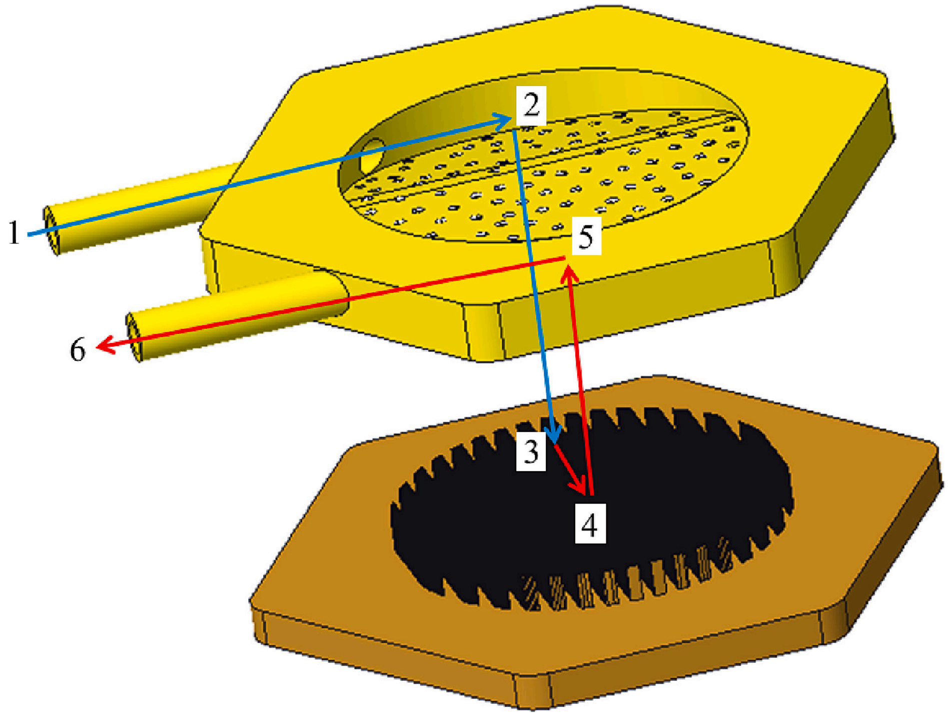

Fig. 5. The schematic of flow path in the cold plate.

Table 2
Geometrical dimension of the original microchannel cold plate

t_b (mm)	h_f (mm)	w_{ch} (mm)	t_f (mm)	D (mm)
3	3	0.1	0.1	26

cold plate is improved by modifying the original cold plate fins and reconfiguring them to pin fin arrays. This study complements a previous investigation [52] aimed at enhancing the commercial Ebullient cold plate performance by altering its channel network geometry and subsequently optimizing the new geometry to minimize thermal and flow resistance.

Three key design parameters, namely h_f (fin height), h_{cf} (height of short fins within mini channels), and w_{mc} (width of machined channels) shown in Fig. 6, are created by machining mini channels perpendicular to the original microchannels. A comprehensive full factorial Design of Experiments (DOE) table (Table 3) has been formulated based on two of these design parameters: width of machined channels (w_{mc}) and fin height (h_f). Each of these two parameters is examined across three different levels, resulting in a total of nine unique design configurations. Additionally, the impact of the height of short fins maintained on the floor of the machined mini channels (h_{cf}) is explored on some of the designs within the full factorial design (h_{cf}). Two grooves, each with a width and depth of 0.76 mm are meticulously machined into the base of the cold plate. These grooves serve as secure installations for T-type thermocouples, enabling the measurement of the average base temperature, T_b (sometimes referred to as wall temperature T_w in two-phase flow terminology) as illustrated in Fig. 4. The T-type thermocouples are calibrated using a precision oven to ensure accurate readings. They are thermally bonded to the grooves using a high-conducting adhesive (8329TFF).

Table 3
Full factorial design table

Design NO.	h_f (mm)	w_{mc} (mm)
1	3	0.5
2	3	1
3	3	2
4	2	0.5
5	2	1
6	2	2
7	1	0.5
8	1	1
9	1	2

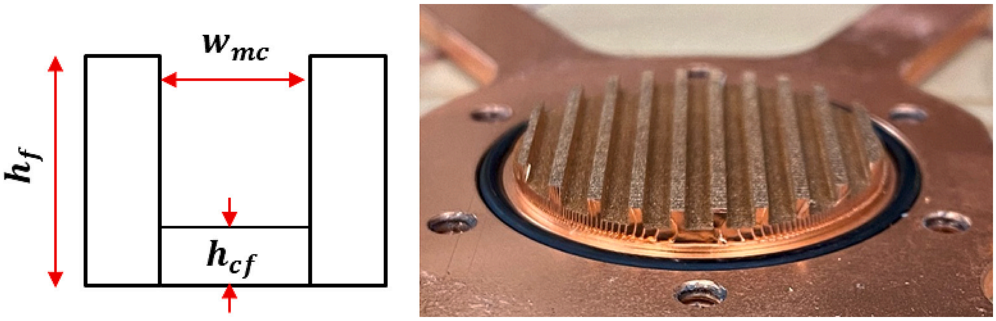

Fig. 6. Modified design with associated design parameters.

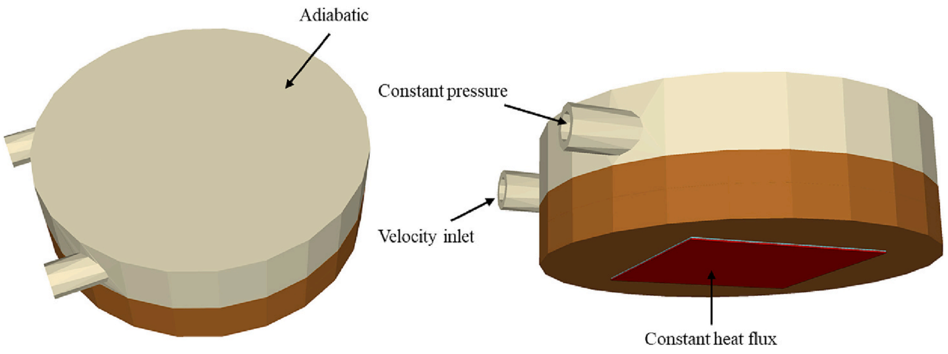

Fig. 7. Computational domain with associated boundary conditions.

2.4. Experimental procedure

A systematic experimental procedure is implemented to conduct tests efficiently. A typical test run, where the heat flux is varied, typically spans 8 to 9 h for completion. The flow is circulated within the test loop through a centrifugal pump. A constant flow rate is regulated by adjusting the DC power supplied to the centrifugal pump. The cold plate's inlet coolant temperature is meticulously controlled by modifying the secondary fluid's inlet temperature within the liquid-liquid heat exchanger via the Julabo LH40 chiller. Before activating the mock heater and commencing data collection, the dielectric coolant is circulated through the system loop at constant flow rate and the desired inlet coolant temperature for about 30 min. This step is crucial to degasify any previously formed and trapped vapor. The air trapped in various components of the loop is directed to the reservoir, eventually rising to the liquid surface and is released into the atmosphere through the vent valve situated at the reservoir's top. While air is being removed, the loop's pressure drops.

The mock block is incrementally heated by adjusting the AC power supply, and data collection begins once the system reaches a steady state. Two T-type thermocouples and two pressure transducers, installed at the inlet and outlet of the cold plate, are employed to measure inlet and outlet temperature and pressure, respectively. It's noteworthy that the coolant enters the cold plate in liquid form and exits as a liquid-vapor mixture. This mixture undergoes condensation back into a liquid state within the heat exchanger before entering the reservoir.

All data acquisition is executed through the National Instrument acquisition system and is compiled into an .xlsx file via a LABVIEW program. The high repeatability consistently observed in the tests underscores the effectiveness and reliability of both the test setup and the test procedure followed.

To maintain consistency, the fluid level in the reservoir is monitored at regular intervals and kept constant throughout all tests. This practice is essential because the fluid fill ratio within the reservoir directly influences the boiling characteristics inside the cold plate, introducing variations in system pressure that affect the dielectric coolant's saturation temperature.

3. Numerical computation

3.1. Basic assumptions

Following assumptions are considered in solving the mass, momentum, and energy equations:

1. A three-dimensional, steady, incompressible, and single-phase flow field is assumed for this study.
2. Negligible effects of gravity, radiation heat transfer, and viscous heat generation are considered.
3. Thermo-physical properties of solid and fluid phases are constant.
4. Turbulent flow conditions are considered.

3.2. Governing equations

The governing equations for a 3D conduction-convection (conjugate) heat transfer problem within an incompressible, steady turbulent flow regime are as follows:

Continuity (mass conservation) equation:

$$\nabla.\vec{V} = 0 \tag{2}$$

In which $\vec{V}$ is the velocity vector field.

Navier-Stokes (momentum) equations:

$$\rho_f\left(\vec{V}.\nabla\right)\vec{V} = -\nabla P + \mu_f + \nabla^2\vec{V} \tag{3}$$

Where $\rho_f$is the density of the fluid, P denotes the pressure field, and $\mu_f$is the absolute viscosity of the fluid.

Energy equation for coolant fluid:

$$\rho_f c_{p,f}\left(\vec{V}.\nabla\right)T_f = k_f\nabla^2 T_f \tag{4}$$

In Eq. (4) $c_{p,f}$ represents the fluid specific heat capacity at constant pressure, T_f is the temperature of the fluid, and k_f stands for fluid conductivity.

The energy equation for solid phases:

$$\nabla^2 T_s = 0 \tag{5}$$

Where T_s represents the temperature of the solid phase.

Turbulent kinetic energy equation:

$$\rho\vec{V}.\nabla k = \nabla.\left(\left(\mu + \rho\frac{c_\mu k^2}{\sigma_k \varepsilon}\right)\nabla \mathrm{k}\right) + \rho c_\mu \frac{k^2}{\varepsilon}\left(\nabla\vec{V} + \left(\nabla\vec{V}\right)^T\right)^2 - \rho\varepsilon \tag{6}$$

The rate of dissipation of turbulent kinetic energy equation:

$$\rho\vec{V}.\nabla\varepsilon = \nabla.\left(\left(\mu + \rho\frac{c_\mu k^2}{\sigma_\varepsilon \varepsilon}\right)\nabla\varepsilon\right) + \rho c_{\varepsilon 1} c_\mu \mathrm{k}\left(\nabla\vec{V} + \left(\nabla\vec{V}\right)^T\right)^2 - \rho c_{\varepsilon 2}\frac{k^2}{\varepsilon} \tag{7}$$

3.3. Numerical domain and boundary conditions

Coolant enters the cold plate through "velocity inlet" and exits it from "pressure constant" outlet. Adiabatic and no-slip boundary conditions are imposed on the side walls and the lid. The lateral surfaces of the fins and the top of the cold plate's spreader, which are in contact with the coolant and participate in heat exchange, are subject to no-slip and thermally coupled boundary conditions. Additionally, constant heat flux is applied to the bottom of the cold plate. Fig. 7 shows associated boundary conditions applied to the computational domain.

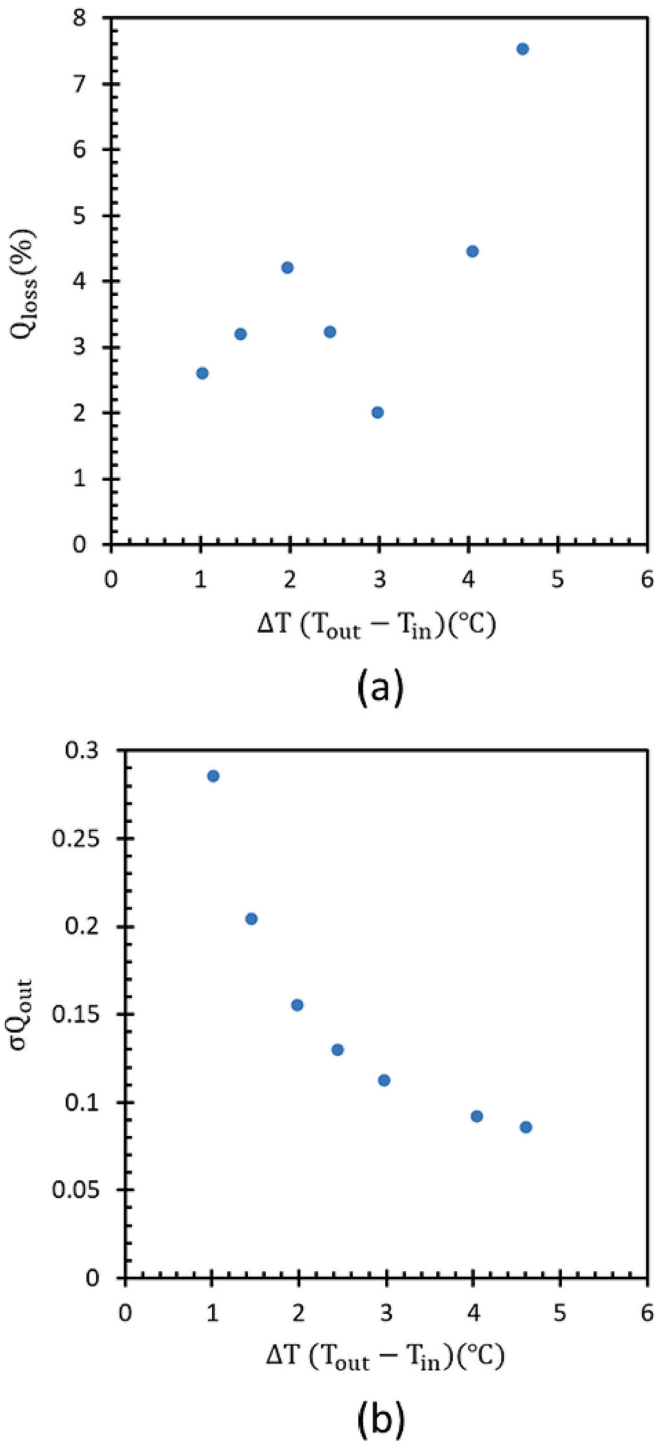

Fig. 8. (a) heat loss versus inlet-outlet temperature difference (b) uncertainty of output power versus inlet-outlet temperature difference at a flow rate of 1.5 LPM

3.4. Numerical approach

Fluid dynamics and heat transfer modeling were conducted using 6SigmaET, an integral component of the 6SigmaDCX software package. This software employs the finite volume method (FVM) to discretize the system of governing equations within the computational domain on a staggered grid. The field of velocity, pressure, and temperature were calculated by solving the system of governing equations using the iterative SIMPLE algorithm. For precise capturing of pressure drop and heat transfer at this scale, 6SigmaET utilizes multi-level unstructured solver. This solver, based on a mathematical formulation incorporating a hierarchy of Cartesian grids and face-to-cell connectivity graph to discretize the differential equations, ensures accurate simulation [53]

4. Heat loss and uncertainty analysis

Multiple tests were conducted under low heat flux conditions (single-phase state) to quantify heat losses.

These losses are determined by measuring the difference between output power (representing sensible heat absorbed by the coolant) and the electrical input power. This approach excludes any discrepancies that might arise from estimating latent heat transfer. The heat loss is estimated by Eq. (8)

$$Q_{loss} = Q_{in} - Q_{out} \tag{8}$$

Where Q_{in} is electrical input power supplied the cartridge heaters, and Q_{out} denotes the sensible heat picked by cold plates and calculated by coolant energy balance (Eq. (9))

$$Q_{out} = \dot{m}c_p(T_{out} - T_{in}) \tag{9}$$

$\dot{m}$ and c_p represent mass flow rate and specific heat capacity of the coolant (Novec7000), respectively. Fig. 8 (a) illustrates the relationship between heat loss and temperature difference at a flow rate of 1.5 LPM. The calculated heat loss is found to be less than 5% of the electrical power input at most data points and less than 8% at the point of maximum heat loss. This graph reveals intriguing findings: at smaller temperature differences, heat loss exhibits fluctuations, while it increases steadily as the temperature difference increases. In assessing the uncertainty associated with measurements, Fig. 8 (b) depicts the uncertainty of output power versus inlet-outlet temperature difference. Notably, the uncertainty of output power exhibits a consistent descending trend with increasing temperature difference, suggesting improved measurement reliability at higher temperature gradients.

The measurement instruments used in the test apparatus are subject to certain uncertainties, as detailed in Table 1. An error analysis, employing the root sum square method [54], has been conducted to calculate the experimental uncertainty of the heat loss and thermal resistance at various heat flux levels, as described in Appendix A. The uncertainty in thermal resistance exhibits a decreasing trend as heat flux increases, diminishing from 13% at a heat flux of 7.3 $\frac{W}{cm^2}$ to 1.6% at a heat flux of 70 $\frac{W}{cm^2}$. A more comprehensive understanding of the uncertainty analysis is presented in Appendix A.

5. Results and discussions

5.1. Operational parameters

5.1.1. Effect of flow rate

This study investigated various operational parameters, including coolant flow rate, coolant inlet temperature, and input heat flux, which vary within the range of 7 to 71 $\frac{W}{cm^2}$. The thermal and hydraulic performances of the cold plate are assessed based on specific thermal resistance and pressure drop, defined by Eqs. (10) and (11), respectively.

$$R_{th} = \frac{(T_b - T_{in})}{q''} \tag{10}$$

In which T_b represents the cold plate base temperature, T_{in} is the coolant inlet temperature, q'' stands for input heat flux.

$$\Delta p = p_{in} - p_{out} \tag{11}$$

Where p_{in} and p_{out} correspond to the pressure at the inlet and outlet of the cold plate, respectively.

The effects of coolant flow rate and heat flux on the thermal per-

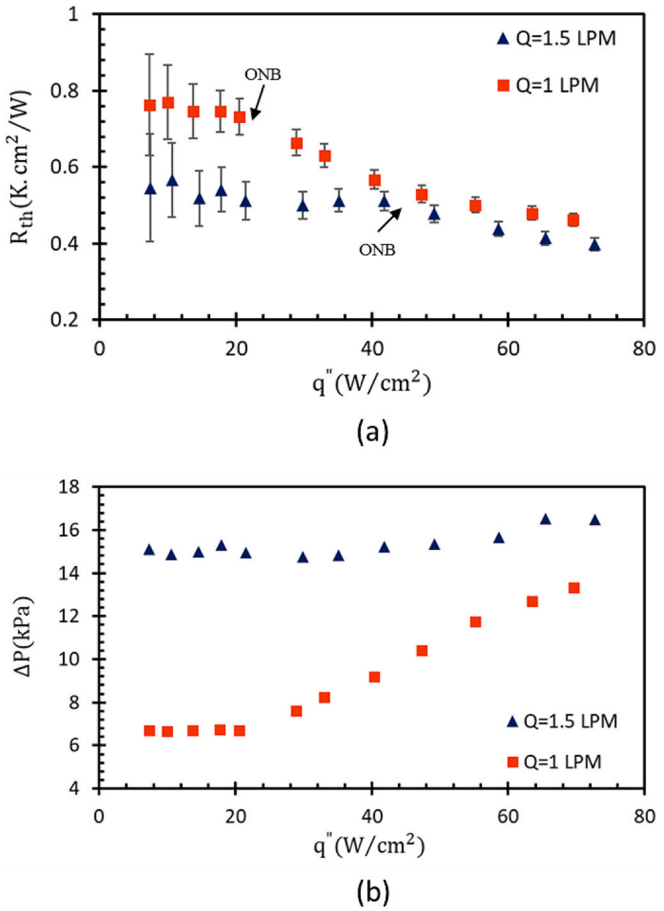

Fig. 9. The effect of flow rate on (a) thermal resistance (b) pressure drop of a design with full fin height of 3 mm and mini channels with width of 1 mm.

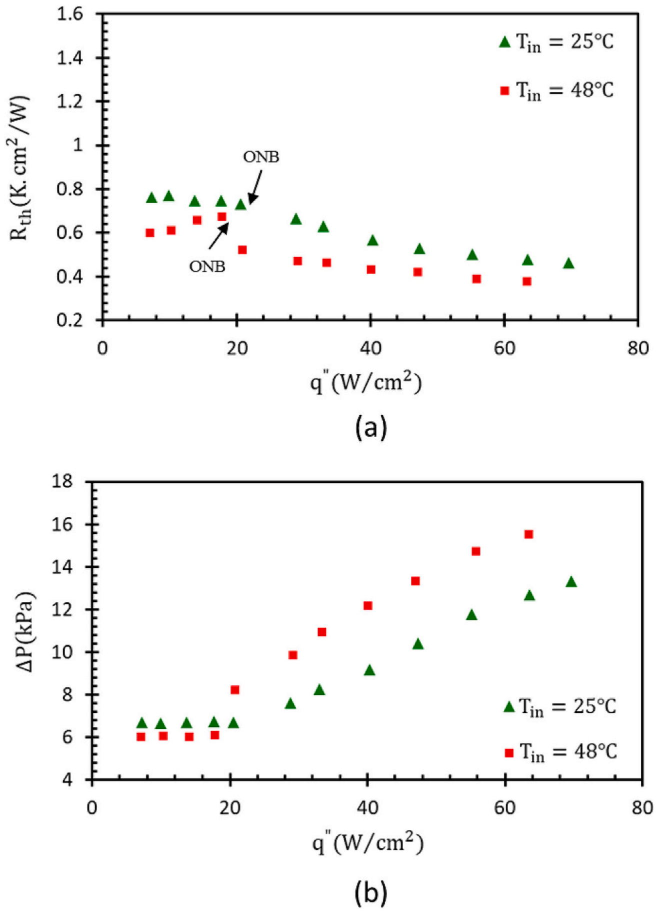

Fig. 10. The effect of inlet temperature on (a) thermal resistance (b) pressure drop of a design with full fin height of 3 mm and machined channels with width of 1 mm

formance of the design with full fin height ($h_f = 3$ mm) and mini channels machined with the width of 1 mm, are shown in Fig. 9 (a). In the initial stage of the heating cycle, characterized by low heat flux conditions where the experiment operates in a single-phase regime, the thermal resistance remains relatively constant irrespective of changes in heat flux. This behavior can be attributed to the fact that, in single-phase flow, thermal resistance is primarily determined by the fluid's ability to receive, store, and carry heat, and heat flux does not affect these abilities significantly. Conversely, increasing the flow rate leads to a reduction in thermal resistance as it increases coolant ability to store heat (decreasing capacity resistance). However, as the onset nucleate boiling (ONB) is reached, thermal resistance starts dropping with heat flux. Beyond the ONB point, higher heat fluxes encourage more vigorous boiling, which enhances the overall heat transfer rate. An increase in flow rate delays the onset of boiling until the mean coolant enthalpy exceeds that of the saturated liquid [55]. However, after the ONB point, when nucleate boiling dominates over single-phase convection, the thermal resistances of two flow rates tend to converge. During periods When nucleate boiling has a substantial influence, cold plate's fin geometry, heat flux, and number of nucleation sites play the key role in determining thermal performance, overshadowing the impact of coolant flow rate [57,58]. Notably, refrigerants, due to their low surface tension and small contact angle, yield bubble departure diameters that are one to two orders of magnitude smaller than those observed with water. Consequently, refrigerants have the capacity to sustain nucleate boiling over a significant portion of the microchannel length, leading to an ascending trend in heat transfer coefficient as heat flux increases [56].

Fig. 9 (b) demonstrates the relationship between pressure drop and heat flux at two different flow rates. In the single-phase regime, the pressure drop is not influenced by changes in heat flux while it significantly rises with increasing flow rate. This can be explained by the fact that in single-phase flow, the pressure drop is primarily determined by frictional losses as the coolant moves through the channels. Increasing the flow rate leads to higher fluid velocity and, consequently, greater frictional resistance, resulting in an increase in device pressure drop. In the two-phase regime, where nucleate boiling occurs, pressure drop increases with both heat flux and flow rate. However, a more interesting observation is that the rate of increase in pressure drop is more pronounced with increasing heat flux at the lower flow rate. Pressure drop and circulation work increase with heat flux as it intensifies bubble generation and flow chaos. At a lower flow rate, the pressure drop increases more sharply with heat flux because nucleation is more dominant. In other words, the formation of bubbles and their subsequent departure from nucleation sites at lower flow rates leads to increased resistance and pressure drop. At higher flow rates, the pressure drop still rises with heat flux but to a lesser extent, as the greater flow rate helps in transporting heat away from nucleation sites more effectively.

5.1.2. *Effect of inlet temperature*

Experiments were conducted at three different coolant inlet temperatures, ranging from 25 °C to 48 °C, in order to investigate the effect of coolant inlet temperature on the boiling characteristics. The flow rate is maintained constant at 1 LPM. Varying the coolant inlet temperature has an equivalent impact on the thermohydraulic performance of various cold plate designs examined in this study. To illustrate the impact of inlet temperature, one of the designs is presented as an example, which is analyzed herein. Thermal resistance and pressure

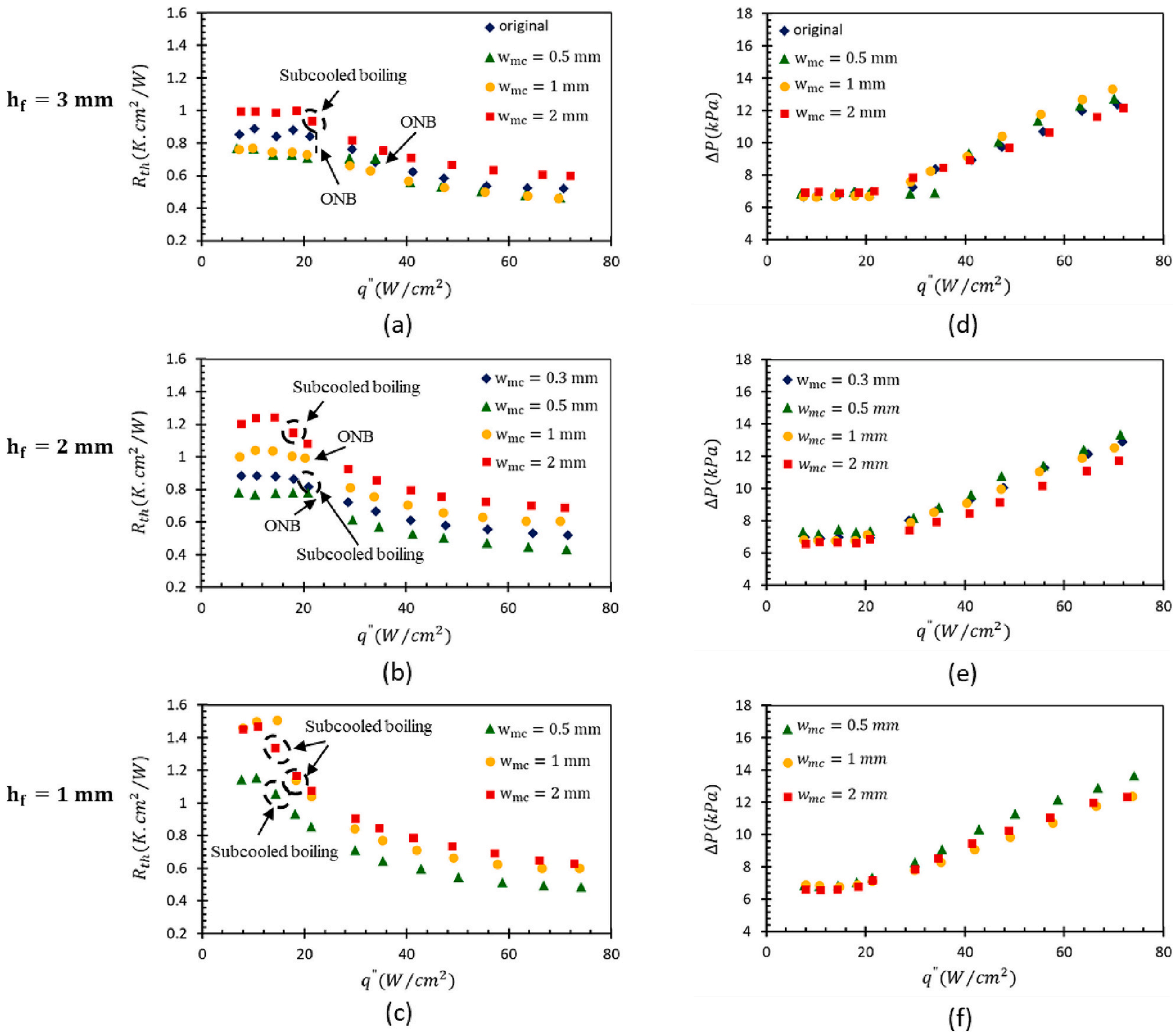

Fig. 11. The effect of machined channels width on (a)(b)(c) thermal resistance (d)(e)(f) pressure drop of designs with different fin heights

drop of the design with $h_f = 3$ mm and $w_{mc} = 1$ mm for two inlet temperatures are presented in Fig. 10 (a) and (b), respectively. Fig. 10 (a) shows that thermal resistance remarkably drops by increasing the inlet temperature from 25 °C to 48 °C in the beginning of the two-phase regime. The reduction in thermal resistance with inlet temperature within this region is attributed to a larger portion of the channel network being engaged in two-phase nucleation boiling at higher inlet temperatures compared to lower inlet temperatures. It is also notable that the ONB heat flux value experiences a slight reduction with a rise in inlet temperature for the same underlying reason. As illustrated in Fig. 10 (a), the thermal resistance values for two inlet temperatures converge as heat flux increases. This convergence is primarily because, at high heat fluxes, a significant portion of the channel network transitions into a two-phase regime, irrespective of the inlet temperature. The coolant inlet temperature exerts contrasting effects on the pressure drop across the cold plate in single-phase and two-phase regimes, as depicted in Fig. 10 (b). In the single-phase regime, the pressure drop decreases slightly with an increase in inlet temperature because of reduction in fluid viscosity with temperature. Conversely, in two-phase regime, the pressure drop significantly rises with inlet temperature. This behavior arises from the elevated number of bubbles generated when the inlet temperature approaches the saturation temperature.

5.2. Geometrical parameters

5.2.1. Effect of machined channel width

A full factorial design (FFD) table (Table 3) is developed using two design parameters, w_{mc} and h_f. Three levels are considered for each design parameter. Therefore, 9 distinct channel network designs are evaluated. These tests are conducted at a consistent flow rate of 1 LPM, spanning three inlet temperatures and encompassing a heat flux range of up to 80 $\frac{W}{cm^2}$. As mentioned in section 5.1.2, the thermohydraulic performance of various cold plate designs tested in this study is uniformly influenced by changes in coolant inlet temperature. Therefore, the subsequent sections of this study will primarily present and analyze the results obtained at $T_{in} = 25^{\circ}$C. Figs. 11 (a) - (c) show the effect of machined channels width across three different fin heights on thermal performance of cold plates. Across all three fin heights, widening the channels leads to an increase in thermal resistance in both single-phase and two-phase regimes due to the loss of both heat transfer surface area and nucleation sites. This increment is more visible for shorter fins compared to full fin height ($h_f = 3$ mm) since shorter fins inherently possess lower heat transfer surfaces area and fewer nucleation sites. As depicted in Fig. 11 (a), the thermal resistance of the original cold plate decreases, in both single-phase and two-phase regimes, when mini

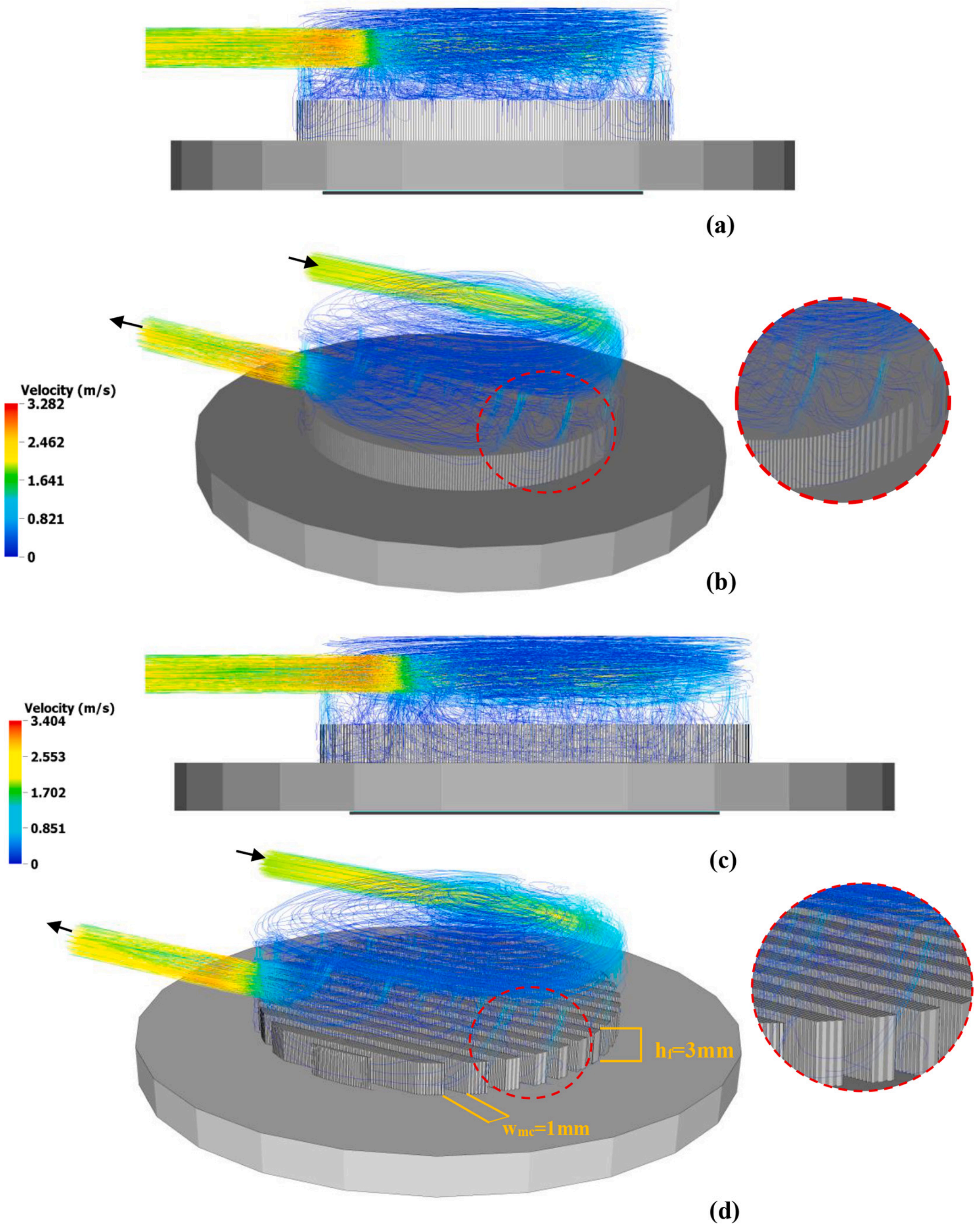

Fig. 12. (a) Lateral view (b) 3D view of streamline patterns in the original cold plate design shown at two different scales of magnification; (c) Lateral View (d) 3D view streamlines in the machined cold plate design with $w_{mc} = 1\ mm, h_f = 3\ mm$ shown at two different scales of magnification.

channels of the width to 1 mm and oriented perpendicular to the original micro channels, are created. Notably, in a two-phase regime, this reduction becomes more pronounced as the heat flux increases. Indeed, in the original cold plate with very narrow channels ($w_{ch} = 0.1$ mm), coolant velocity is very low close to the channels floor. It could be considered as creeping flow at the root of fins, resulting in conduction superiority over convection. However, by incorporating the mini channels, the coolant flows at elevated velocity near the root of the fins and channels floor, thereby enhancing the overall heat transfer performance. To understand the impact of mini channels on fluid flow behavior, computational simulations were executed for both the original design and machined designs. Fig. 12 displays the associated streamline patterns. The CFD models show, in both lateral and 3D views, that the flow gets closer to the channel roots in the machined design. In contrast, the original configuration has limited flow access to these areas. Removing more portion of fins by creating wide channels $w_{mc} = 2$ mm, however, reversely increases thermal resistance to higher than the original design's due to the significant loss of heat transfer surface area and nucleation sites. As the design with $w_{mc} = 0.5$ mm and $h_f = 2$ mm outperforms all other full factorial table designs, authors tested a design (out of FFD table) with $w_{mc} = 0.3$ mm and $h_f = 2$ mm to investigate whether narrower mini channels than 0.5 mm enhances thermal resistance. As Fig. 11 (b) shows, thermal performance decreases by decreasing the machined channel width from 0.5 mm to 0.3 mm. The effect of w_{mc} on hydraulic performance of the cold plates is demonstrated in Fig. 11 (d) – (f). As Fig. 11 (d) shows, by creating the channels of the width of 0.5 mm and 1 mm pressure drop slightly increases as, unlike the original design, the high velocity flow cannot skip the regions

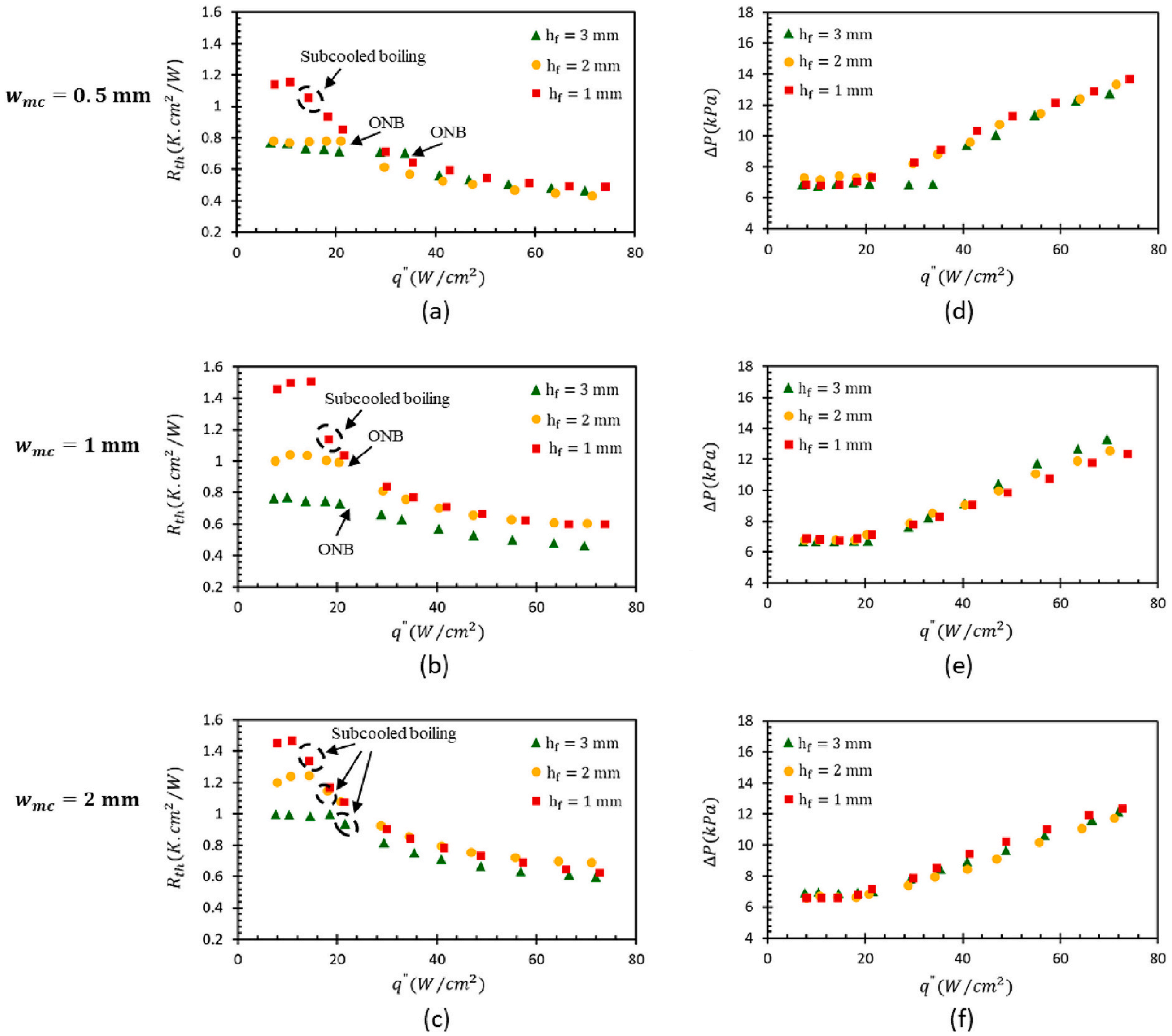

Fig. 13. The effect of fin height on (a)(b)(c) thermal resistance (d)(e)(f) pressure drop of designs with different machined channels widths

closed to the root of fins and channels floor. As expected, pressure drop moderately reduces by widening the mini channels due to lower flow velocity and fluid-solid contact area.

As depicted in Fig. 11, particularly Fig. 11 (c), a notable decrease in thermal resistance is observed with minimal change in pressure drop within the heat flux range of 15 to 20 $\frac{W}{cm^2}$. This observation suggests the potential occurrence of the subcooled boiling phenomenon. Subcooled boiling is characterized by the fluid temperature remaining below the saturation point, leading to the condensation of vapor formed at superheated walls upon contact with the colder bulk fluid. This process generates small bubbles near the channel walls. In contrast to single-phase flow, subcooled boiling exhibits a disproportionate increase in temperature difference between the base and inlet (numerator of thermal resistance definition, Eq. 10) compared to power (denominator of Eq. 10) due to the formation of tiny bubbles. Consequently, thermal resistance decreases with increasing power, while pressure drop remains relatively constant, consistent with observations reported in the literature [59]. Our findings suggest that the visibility of subcooled boiling depends on the aspect ratio of the channels and inlet temperature.

5.2.2. *Effect of fin height*

The FFD test results are once again demonstrated in Fig. 13 (a) – (c), this time with a different orientation, to investigate the effect of fin height on the thermal performance of the cold plate for three different machined channel widths. In single-phase regime, thermal resistance significantly rises with shortening the fin height because of the loss of heat transfer surface area. However, in narrow machined channels with the width of 0.5 mm thermal resistance remains almost constant by shortening the fins from 3 mm to 2 mm. This can be attributed to a balance between the effect of heat transfer surface area reduction and flow velocity rise which effectively cancels out any significant change in thermal resistance. In two-phase regime, designs with different width of machined channels perform differently with shortening the fins since both heat transfer surface area and nucleation are contributing to heat transfer. In narrow machined channels ($w_{mc} = 0.5$ mm), although heat transfer surface area reduces with decreasing the fin height from 3 mm to 2 mm, flow velocity and nucleation sites increase at the root of the fins. The effect of larger nucleation sites overcomes the effect of heat transfer surface area reduction and as a result thermal resistance slightly decreases. Further reduction in fin height to 1 mm causes lower flow velocity and fewer nucleation sites at the root of the fins besides less heat transfer surface area which results in higher thermal resistance. In wider machined channels designs, $w_{mc} = 1$ mm and $w_{mc} = 2$ mm, that coolant effortlessly flows at the root of the fins, shortening the fin height from 3 mm to 2 mm decreases flow velocity, heat transfer surface area, and nucleation sites which results in thermal resistance rise. Thermal performance does not change with further reduction in fin height to 1 mm.

As it is observed in Fig. 13 (d) – (f), pressure drop does not show remarkable sensitivity to the fin height. To better understand the

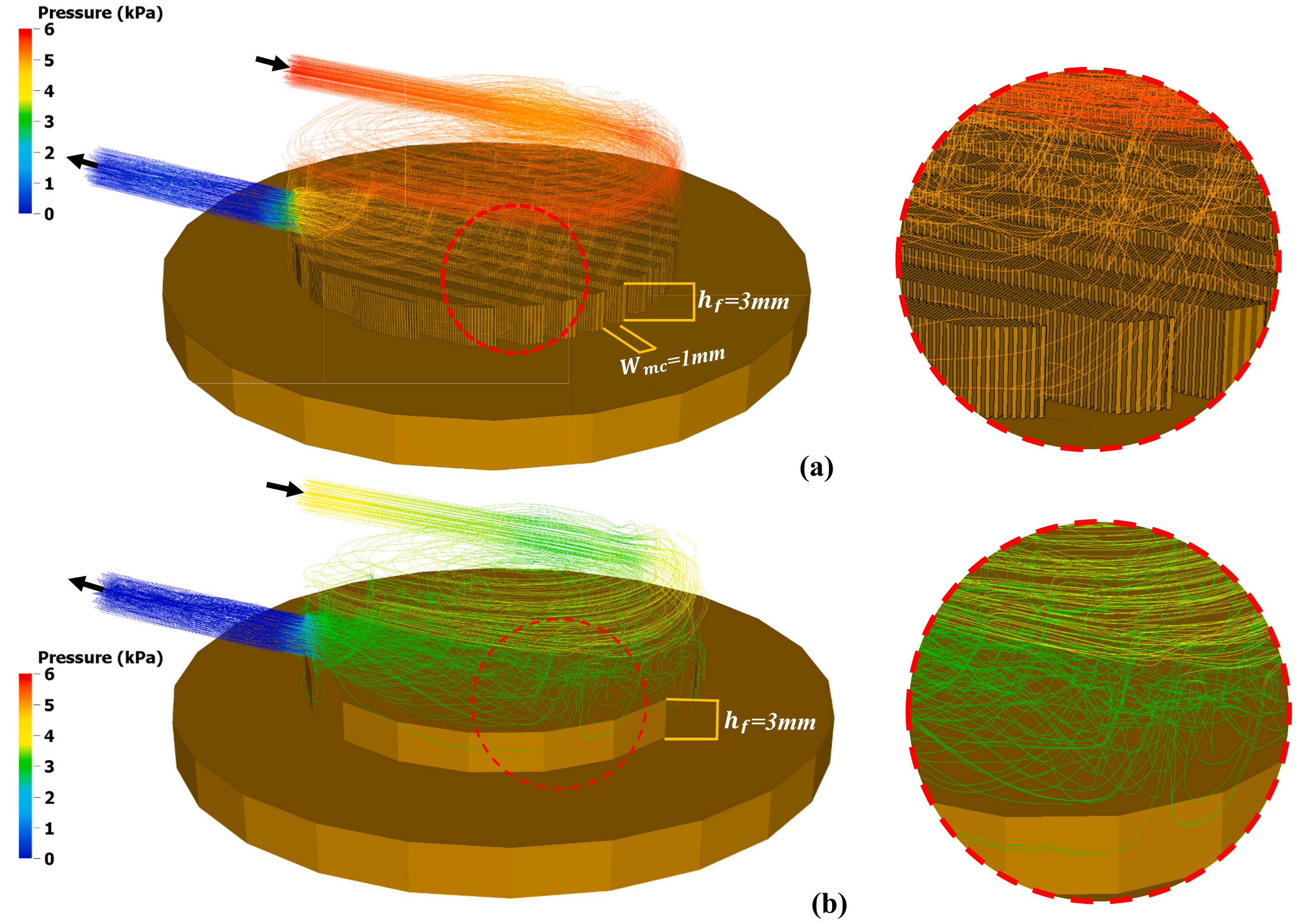

Fig. 14. Pressure changes along the streamlines in the CFD models with (a) microchannels $h_f = 3$ mm $h_{cf} = 1$ mm (b) no channels illustrated with two levels of magnification.

individual influences of the manifold and microchannel (fin geometry) on pressure drop, two compact models were developed and compared: one model with integrated microchannels within the cold plate ($w_{mc} = 1$ mm, $h_f = 3$ mm), whereas the other model lacks any fins. Ensuring the manifold dimensions remained constant in two models enables us to accurately quantify the pressure reduction solely attributed to the microchannels. A comparison between the experimental and simulation model results reveals an approximate 4% discrepancy, demonstrating good agreement between the two.

The single-phase simulation has been conducted, at $T_{in} = 25^{\circ}$C and $Q = 1$ LPM. By conducting these models' comparison, we gained valuable insights into the exact portion of pressure drop occurring within the microchannels. Fig. 14 shows the pressure change along the streamlines in both cases. It is concluded that 70% of the total pressure drop occurs in manifold. This is the reason why pressure drop does not show sensitivity to different fin network designs.

5.2.3. *Effect of short fins through created channels*

At the next step of geometry optimization, short fins are preserved through the created channels rather than removing the whole fins to the base surface (shown in Fig. 6). The effect of these fins' height (h_{cf}) on the thermo-hydraulic performance of the cold plate is investigated and demonstrated in Fig. 15 (a) – (h). Starting from $h_f = 3$ mm, preserving short fins to the height of 0.5 mm through the machined channels with $w_{mc} = 2$ mm improves thermal performance in both single-phase and two-phase regimes due to heat transfer surface area and nucleation sites increase. However, higher fins with height of 1 mm through machined channels have adverse effect on thermal performance since they hinder coolant to flow, and nucleation sites to form at the root of the fins. Fig. 16 presents single-phase simulation outcomes for two streamlined models, both with a microchannel width of 2 mm and a fin height of 3 mm but differing in short fin heights of 0.5 mm and 1 mm. The data indicates that fluid flow is more noticeable near the channel roots in the 0.5 mm case, while the 1 mm configuration shows reduced fluid access to these areas.

In narrower machined channels ($w_{mc} = 1$ mm, Fig. 15 (b)), even short fins with the height of 0.5 mm decreases thermal performance of the cold plate. Consequently, it is expected that short fins through the $w_{mc} = 0.5$ mm increases thermal resistance as flow velocity is already low at the root of the fins and short fins in machined channels make it worse. Like $h_f = 3$ mm, in $h_f = 2$ mm with wide machined channels ($w_{mc} = 2$ mm) maintaining short fins with $h_{cf} = 0.5$ mm through the machined channels decreases thermal resistance while higher channel fins adversely affect thermal performance of the cold plate. Based on the results obtained, no improvement is anticipated for the rest of full factorial designs with short fins through the machined channels. As shown in Fig. 15 (e) – (h), again pressure drop does not show considerable sensitivity to the short fins through the machined channels.

In summary, while incorporating short fins ($h_{cf} = 0.5$ mm) in the wide mini channels ($w_{mc} = 2$ mm) improves the thermal performance of the cold plate compared to designs featuring wide mini channels without short fins, the design with $w_{mc} = 0.5$ mm, $h_f = 2$ mm, and no short fins in the mini channels emerges as the optimal configuration, outperforming all other designs.

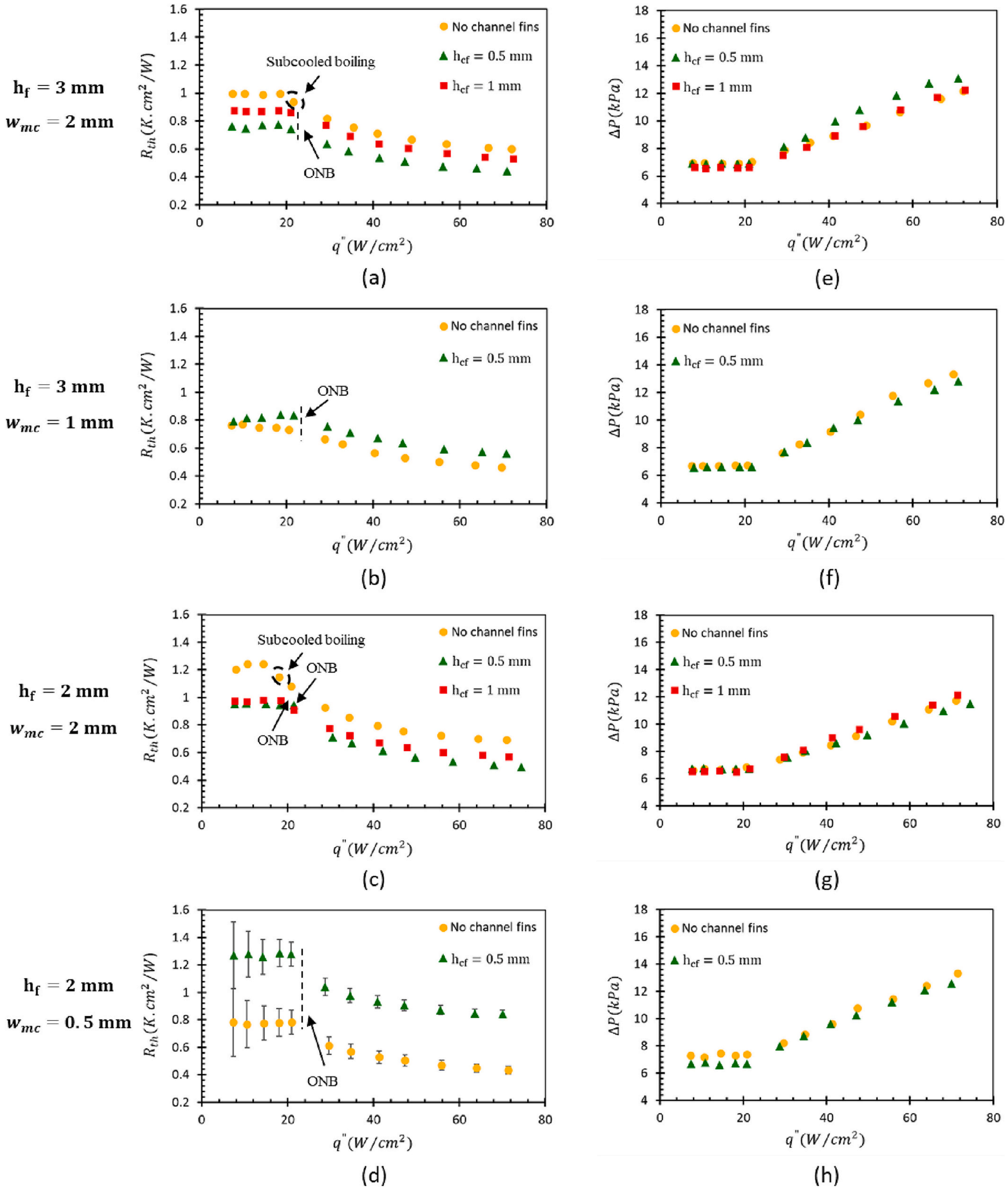

Fig. 15. The effect of short fins through machined channels on (a)(b)(c)(d) thermal resistance (e)(f)(g)(h) pressure drop of cold plate

$h_{cf} = 0.5$ mm presented at two magnification levels (c) Side view (d) 3D view of streamlines in compact model with $w_{mc} = 2$ mm $h_f = 3$ mm $h_{cf} = 1$ mm presented at two magnification levels

5.3. Artificial neural network-based compact model for two-phase flow boiling

In this manuscript, we have demonstrated a compact model based on multi-layer Neural Network for a specific geometry of cold plate under

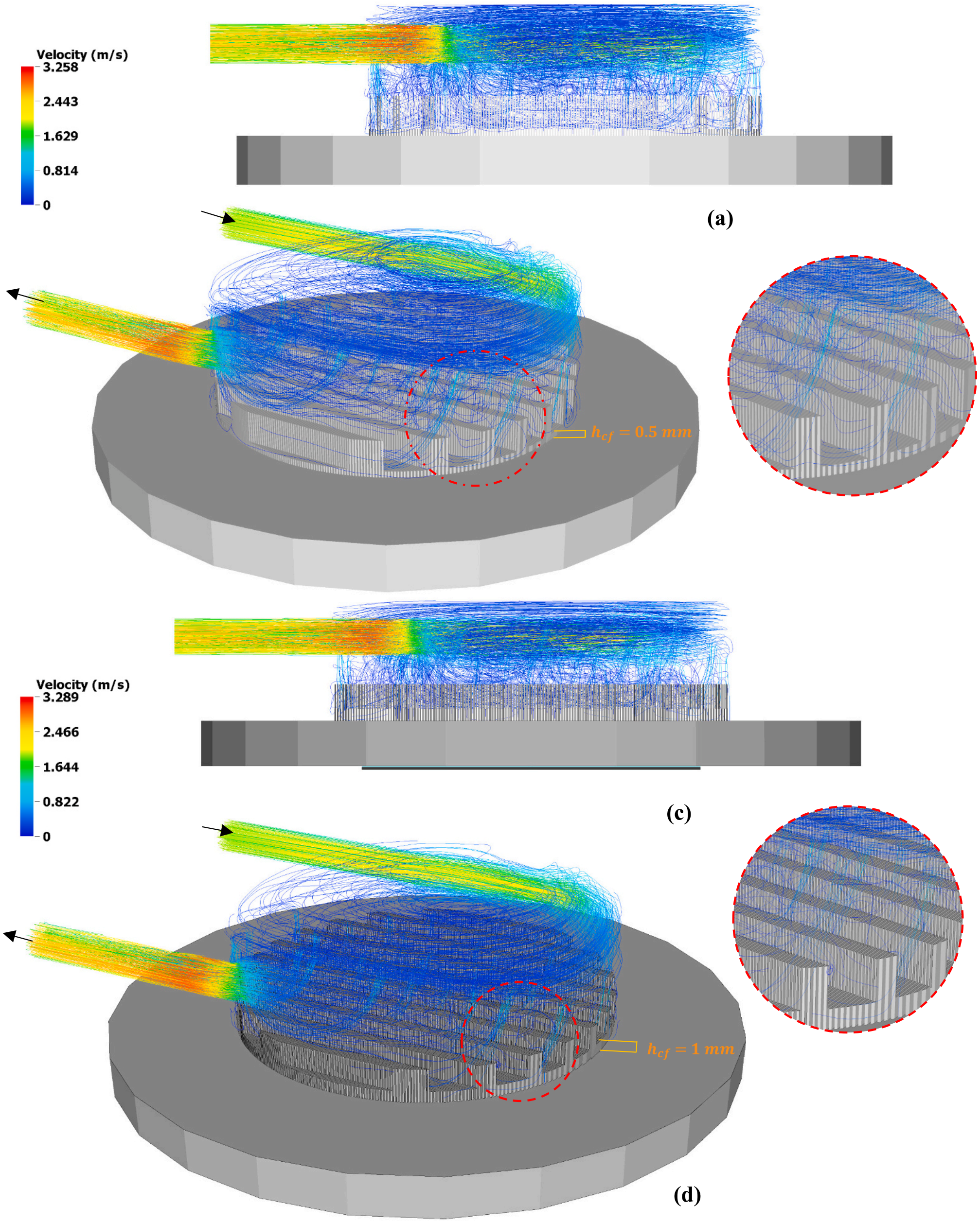

Fig. 16. (a) Side view (b) 3D view of streamlines in compact model with $w_{mc} = 2$ mm, $h_f = 3$ mm

the fixed operating condition of flow (Flow rate = 1 LPM and $T_{in} = 25^{\circ}C$) and heat flux. It is important to note that from the in-house experimental results (discussed in the previous sections), T_{in} has a monotonic effect on the cold plate performance both in single and two phase.

The compact model developed aims to predict to five characteristics of the cold plate geometry namely,

1. Single-phase thermal resistance
2. Single-phase flow pressure drops
3. Two-phase thermal resistance at 70 W/cm^2
4. Two-phase pressure drops at 70 W/cm^2
5. Heat flux corresponding to Onset of Nucleate Boiling (Marks the departure from Single to two-phase flow regime)

There have been many studies for developing empirical correlations [60,61] to predict the heat transfer coefficient and critical heat flux in microchannel and pin fins. Usually, conventional regression models are used to find relationships between Geometric parameters, operating conditions, and heat transfer coefficients. From the reported studies it was also evident that the conventional regression models cannot accurately capture the microchannel's geometrical and fluid flow physics. Therefore, we adopted a multiple hidden layer (Deep learning) based on artificial neural network (ANN) that is widely used to model complex interdependent parameters. Training our deep learning model with our carefully collected experimental dataset allows for an accurate prediction of single and two-phase thermos hydraulic performance and the heat flux corresponding to onset of Nucleate Boiling for a fixed flow condition. Fig. 17 shows the architecture of our Artificial Neural Network with weights, bias, layers, functions, and optimizer.

Furthermore, to improve the prediction capability, we also have an option to optimize the number of hidden layers in the ANN model. The number of hidden layers and number of hidden neurons in each hidden layer play a vital role during the backpropagation process to readjust the

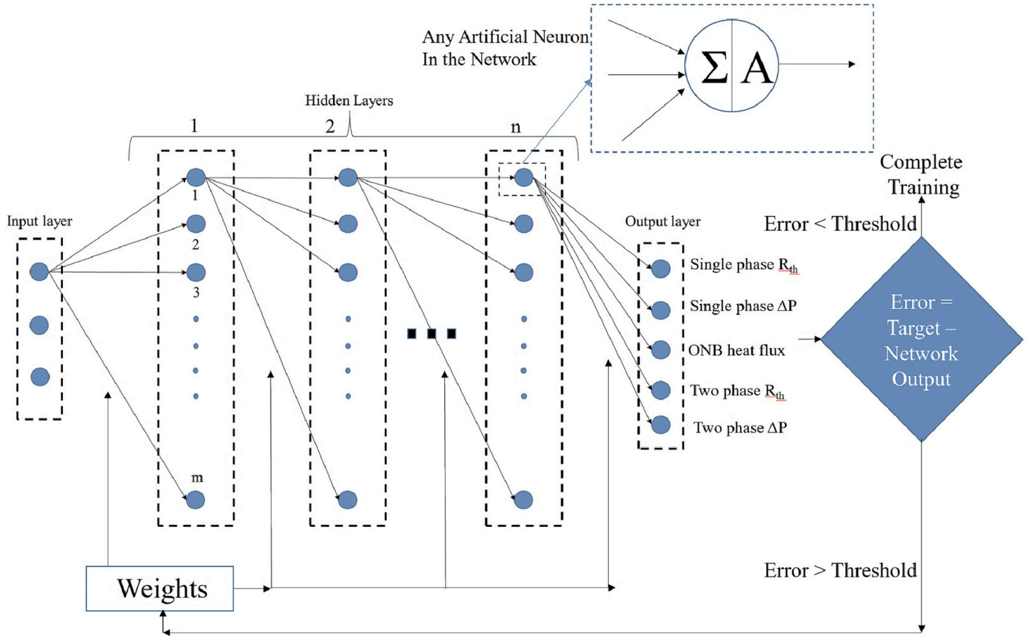

Fig. 17. Architecture of the deep learning based Artificial Neural Network employed in the study. "n" denotes the number of hidden layers and "m" denotes the number of hidden neurons in each layer." A" denotes the nonlinear activation function (Note: A fully connected network is employed)

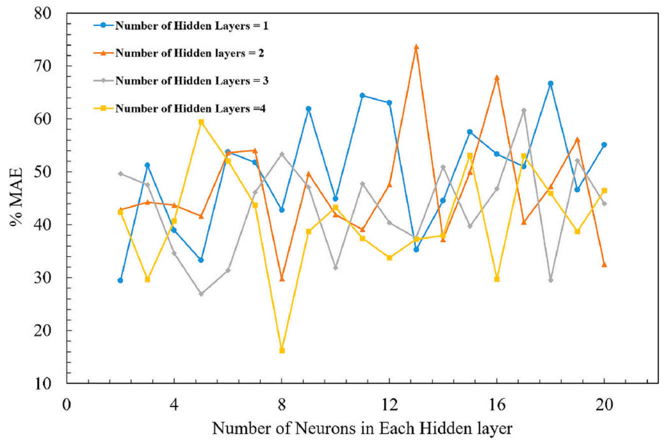

Fig. 18. Results from the parametric study of the hyperparameters employed in the MLP based ANN

network weights. The procedure to select the network architecture mainly depends on the size of the data, spread of the data and number of input and response variables. The number of nodes in each layer is selected heuristically as there is no rule of thumb that dictates the required number of hidden layers in a neural network. The Levenberg Marquardt technique is employed as the optimizer tool to arrive at optimized hyper parameters of the deep learning-based ANN during the backpropagation. Deep learning based Artificial Neural Network model minimizes the cost function (Y_{pred} - Y_{exp}) with $Y_{pred} = XW + b$. X is the input parameter of the data, W the weight, and b the bias. The initialization of the weights was carried out using the Nguyen-Widrow method, which works well for Tan Sigmoid function and bias is initialized to zero. The weights are updated using the Levenberg Marquadt algorithms, which is a classical back propagation algorithm used in the artificial neural network.

The hyperparameters of ANN, namely the numbers of hidden layers and nodes per layer, were chosen from different combinations of hidden layers and nodes per layer based on the predictive accuracy of the validation set after training the ANN on the training set. The results of the optimized hyperparameters are shown in Fig. 18. The experimentally obtained data were randomly divided into three groups, 72% of the data was employed for training, 18% for validation and 10% for testing and then the predictive accuracies with different numbers of layers and nodes combinations were determined using mean absolute error (MAE) of the validation set. Fig. 19 reports the final accuracy of prediction using the test dataset.

Fig. 18 shows validation MAEs for different combinations of numbers of hidden layers and nodes per each hidden layer. For this study, the combinations of 4 layers and 8 hidden Neurons in each hidden layer set is adopted since it shows the low validation MAE.

Fig. 19 (a) and (b) show the Parity plot for the training and testing data for single and two-phase flow scenarios.

5.4. *Artificial neural network driven optimization*

The optimization problem could be stated mathematically as

$$\textit{Maximize}\ R_{th} = f\left(h_f, w_{mc}, h_{cf}\right)$$

$$\textit{Minimize}\Delta p = f\left(h_f, w_{mc}, h_{cf}\right)$$

The compact model developed using the multi-layer ANN is employed as the objective function for the optimization problem and directly coupled to the optimization engine. From the experimental data, it is observed that, for the single-phase flow, the variation of pressure drops in the microchannel is within the uncertainty of the measured data. Reiterating the fact that over 70% of the pressure drop occurs in the manifold [49], the geometry variation did not yield significant variation in pressured drop as the same manifold design was used for all of the different microchannel designs. The variation in pressure drop in the range of microchannel geometry considered is so negligible that the entire optimization for single phase flow can be treated as a single objective optimization leading to one single global optimal that has the minimum thermal resistance. Hence, we employed the classical Genetic Algorithms (GAs) for the single objective optimization. Genetic Algorithms (GAs) [61] are a class of stochastic optimization algorithms inspired by the process of natural selection. GA is commonly employed for obtaining a global optimal solution for multivariable multiple constraint optimization problems. The flow chart of

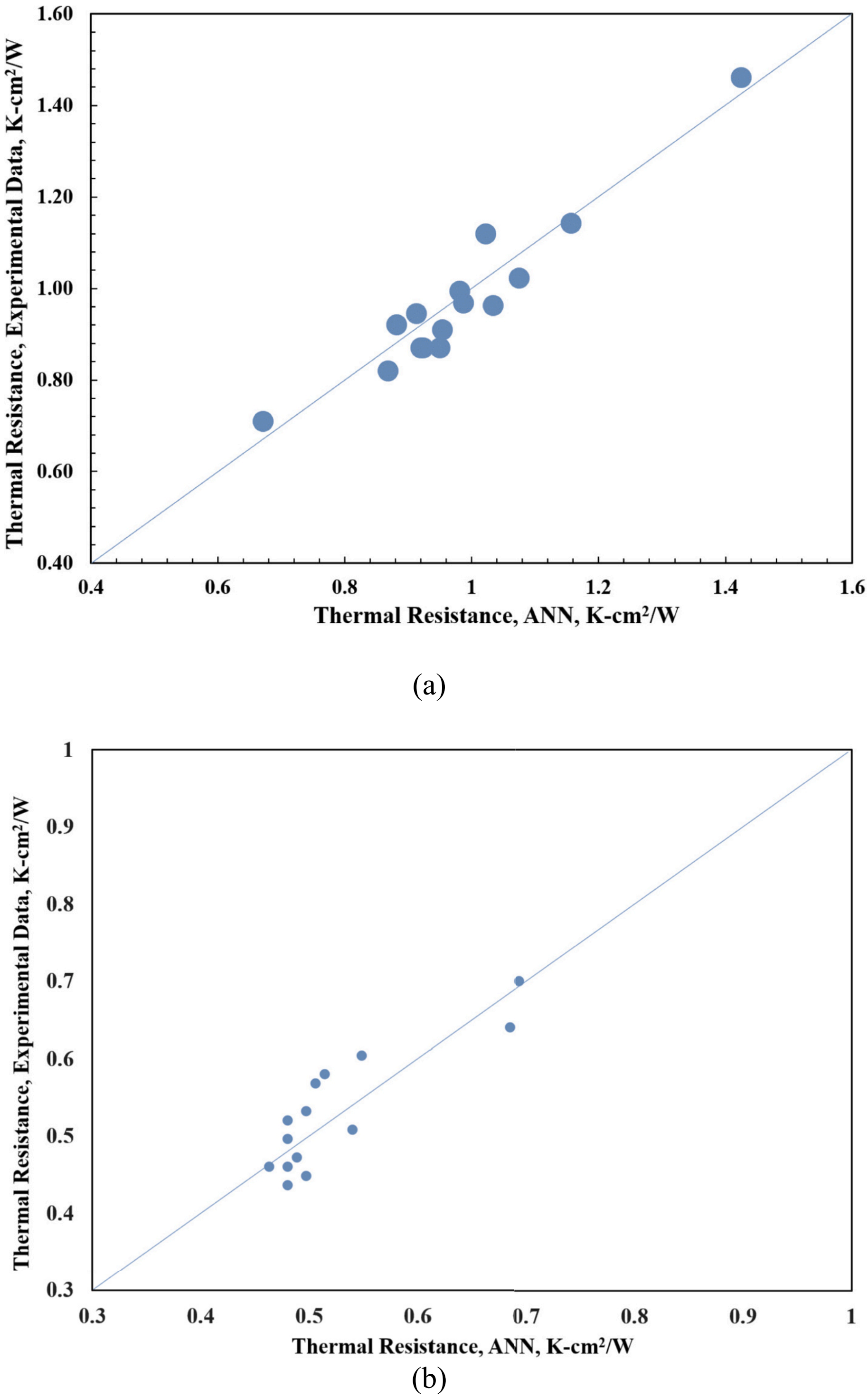

Fig. 19. Parity plot for testing data from the MLP based compact models for prediction of thermal resistance of (a) single phase cooling (b) two phase cooling

GA is as shown in Fig. 20. The parameters that govern the output of the algorithm are the rate of crossover and mutation are the probability of crossover P_c and the probability of mutation P_m .

A sensitivity analysis is performed to determine the optimal values of P_c and P_m . The configuration with fin height $h_f = 3\,mm$, machined channel width $w_{mc} = 2\,mm$ and channel fin height $h_{cf} = 0.5\,mm$ is determined to be the global optimal. For the two-phase flow, a detailed multi-objective optimization is carried out using the non-dominated sorting Genetic Algorithm – II [62,63].

The primary advantage of the algorithm compared the traditional genetic Algorithm is the preservation of both elitism and diversity in the obtained solutions. NSGA-II is a stochastic search-based optimization algorithm that requires the evaluation of objective function in each iteration. Therefore, the algorithm requires a more robust objective function to achieve global optimal solutions. Output of NSGA-II is sensitive to the optimization parameters such as the probability of mutation and the probability of cross-over. A detailed sensitivity analysis [49] was performed, and it was determined that $Pc = 0.65$ and $Pm = 0.15$ gave more robust results. A detailed description of the algorithm and its application to heat transfer problems can be found in [39]. The trade-off

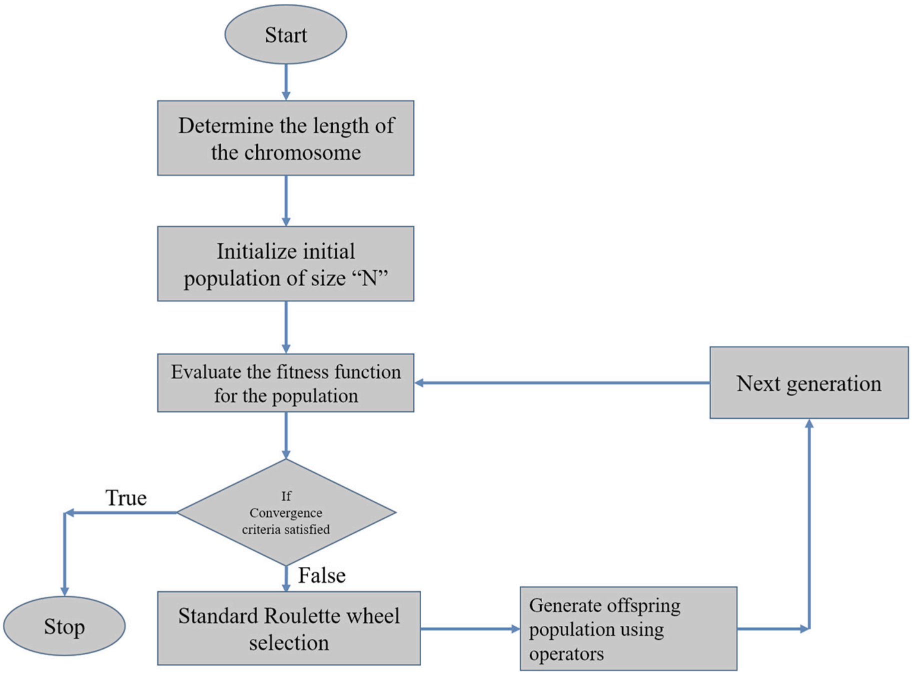

Fig. 20. Flowchart for the Genetic Algorithm

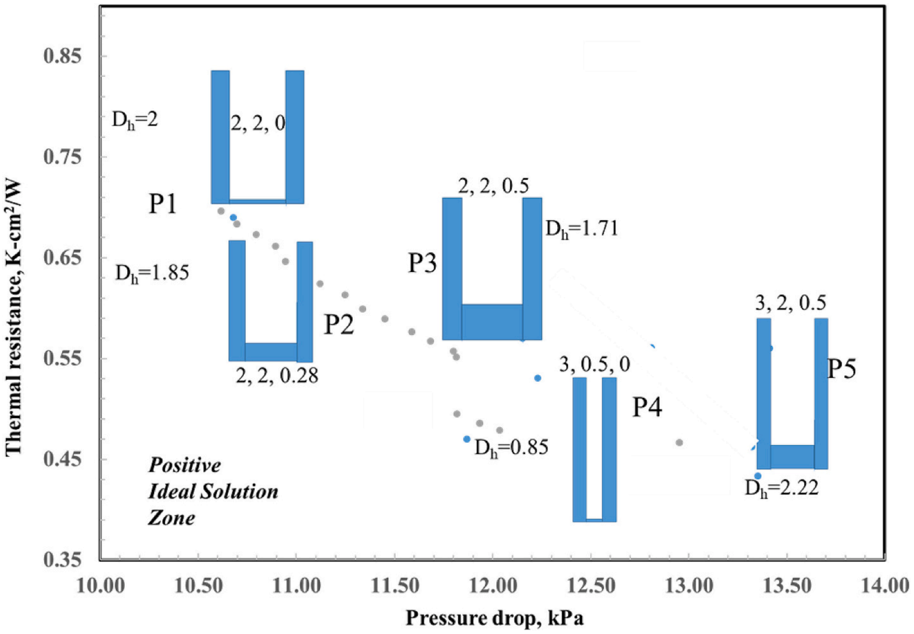

Fig. 21. Pareto optimal solutions for the two-phase flow boiling in microchannels at 70 $\frac{W}{cm^2}$, $T_{in} = 25^{\circ}$C and flow rate of 1 LPM. The values adjacent to each design represents fin height h_f, machined channel width w_{mc} and channel fin height h_{cf} in this specified order

is represented as a Pareto optimal plot shown in Fig. 21.

The designs P_1, P_2, P_3, P_4, P_5 are the five Pareto optimal solutions reported in this study. As we progress from Design P_1 to P_5 there is a considerable reduction in thermal resistance and increase in pressure drop simultaneously. We require a higher-level information to choose one best design from all of the Pareto optimal design. For instance, if thermal resistance has to be minimized and pressure drop has no limitation/constrained, Design P_5 is the Global optimal design. However, if pressure drop is desired to be minimized and thermal resistance is not given any weightage, then design P_1 becomes the optimal. If both thermal resistance and pressure drop are given equal weightage design P_2 and P_3 will become the global optimal design. In such a scenario design P_2 is very interesting. It is to be noted that design P_2 was identified by the compact model-based optimization.

6. Conclusion

In this study, the thermo–hydraulic performance of a commercial two-phase microchannel multi-jet impingement cold plate was investigated and improved by making changes in its architecture. Then the reformed design was optimized in dimensions using neural network. The major conclusions from this study are as follows:

i. Thermal resistance decreases with heat flux in two-phase flow regime where nucleate boiling is dominant as expected.
ii. Thermal resistance drops with flow rate in single-phase and subcooled boiling regions while it is rarely dependent on flow rate in nucleate boiling region.
iii. Increasing coolant temperature results in a higher bubble generation rate and lower thermal resistance consequently.
iv. Machining channels to the width of 1 mm perpendicular to the original micro channels improved thermal performance of the cold plate while pressure drop slightly increased.
v. Unlike in single phase heat sinks where heat transfer surface area plays an important role in determining thermal and flow performance, in two-phase heat sinks, due to the high convection coefficient, flow pattern and number of bubble sites determine the performance of the device.

- In the original design, creeping flow occurs on the base of the channel network due to the very narrow channels. This creeping flow results in pool boiling at the root of the fins. By creating mini channels perpendicular the original ones, coolant can flow at the root of the fins easily and pool boiling is replaced by convective boiling which results in higher thermal performance.
- Moreover, creating mini channels increases number of bubble sites resulting in higher bubble generation rate and thermal improvement.
- The optimized design with a mini channel width (w_{mc}) of 0.5 mm and fin height (h_f) of 2 mm exhibited a notable 17% improvement in thermal performance compared to the original design.
- Machining channels does not result in any significant pressure drop penalty. Creating channels to the original channel network from one side increases the bubble generation rate and on the other side reduces solid-liquid contact area. The effect of these changes cancels each other out which leads to insignificant change in pressure drop.
- Despite a modest 7% increase in pressure drop from 12.4 to 13.3 kPa with the optimized design, it remains well within an acceptable range for practical applications. This minor increment in pressure drop ensures adequate fluid flow and system operation, underscoring the balance achieved between thermal efficiency and hydraulic performance.
- In improving cold plate performance, there is a trade-off between heat transfer surface area and flow velocity and number of bubble sites. In other words, by creating very wide (2 mm) channels or excessively shortening the fins we lose a large amount of heat transfer surface area which results in adverse effect on thermal performance.

vi. Deep learning based compact model was developed for predicting the performance of the cold plate under single and two-phase operating regime with a mean absolute error of less than 10%.
vii. The compact model based single and multi-objective optimization of the cold plate was successfully demonstrated. The optimization was able to identify both the best and worse design recommendations for single and two-phase regimes. The results from optimization can be utilized as a design guideline chart when we wish to choose optimal solution based on the preference between the desired thermal resistance and pressure drop.

This study paves way for future optimization studies on pumped two-phase flow boiling.

CRediT authorship contribution statement

Najmeh Fallahtafti: Writing – review & editing, Formal analysis, Data curation, Conceptualization. **Farzaneh Hosseini:** Writing – review & editing. **Yaser Hadad:** Writing – review & editing, Conceptualization. **Srikanth Rangarajan:** Writing – review & editing, Methodology. **Cong Hiep Hoang:** Conceptualization. **Bahgat Sammakia:** Supervision, Project administration, Funding acquisition.

Declaration of competing interest

The authors declare the following financial interests/personal relationships which may be considered as potential competing interests:

Bahgat Sammakia reports financial support was provided by Semiconductor Research Corp. If there are other authors, they declare that they have no known competing financial interests or personal relationships that could have appeared to influence the work reported in this paper.

Data availability

Data will be made available on request.

Acknowledgement

This work is supported by SRC (Task 2878.006). S.N.S. acknowledges the NSF Award IIP-1738793 and the Integrated Electronics Engineering Center (IEEC) at the State University of New York at Binghamton. The IEEC is a New York State Center for Advanced Technology with funding from New York State through the Empire State Development Corporation.

Appendix A

The uncertainty of thermal resistance in this article is calculated employing Root Sum Square method defined by Eq. (A_1).

$$\sigma R = \left\{ \sum_{i=1}^{N} \left(\frac{\partial R}{\partial X_i} \times \Delta X_i \right)^2 \right\}^{\frac{1}{2}} \quad (A1)$$

Each term in Eq. (A_1) represents the contribution of one variable (X_i) uncertainty in the total uncertainty (σR). Thermal resistance is calculated from Eq. 4 where q is obtained from Fourier law (Eq. 1). In Eq. 1 $\Delta T = T_{bot} - T_{top}$ which is temperature difference measured by thermocouples located at the bottom and top of mock heater neck shown in Fig. A1, and Δx is the distance between these two thermocouples. Substituting q from Eq. 1 in Eq. 4, the Eq. (A_2) for thermal resistance is obtained.

$$R_{th} = \frac{(T_b - T_{in})\Delta x}{K(T_{bot} - T_{top})} = \frac{\Delta x \times \Delta T_{b-in}}{K \times \Delta T_{bot-top}} \quad (A2)$$

Eq. A_3 for total uncertainty is obtained by applying the basic equation of uncertainty analysis (A_1) to thermal resistance (Eq. A_2) with 3 variables of Δx, ΔT_{b-in}, and $\Delta T_{bot-top}$.

$$\sigma R_{th} = \sqrt{\left(\frac{\sigma \Delta x}{\Delta x}\right)^2 + \left(\frac{\sigma \Delta T_{b-in}}{\Delta T_{b-in}}\right)^2 + \left(\frac{\sigma \Delta T_{bot-top}}{\Delta T_{bot-top}}\right)^2} \tag{A3}$$

Where $\sigma \Delta T_{b-in} = \sigma \Delta T_{bot-top} = \sqrt{2 \times (\sigma T)^2}$, since the uncertainty of all thermocouples are equal. The Table A1 shows the values of Δx, ΔT_{b-in}, and $\Delta T_{bot-top}$, their uncertainty intervals, and thermal resistance uncertainty for the experiment of the design with fin height of 3 mm and machined channels width of 1 mm at inlet temperature of 25°C and flow rate of 1 LPM

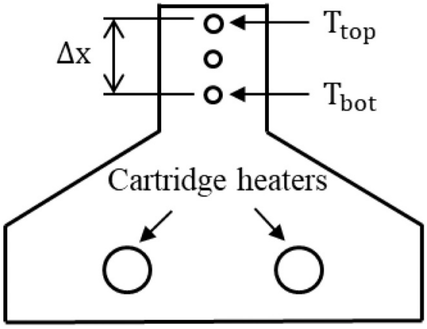

Fig. A1. Schematic of the copper block and position of thermocouples used for measuring heat flux

Table A1
Values of 3 variables and their uncertainty intervals and thermal resistance uncertainty of a design with fin height of 3 mm and machined channels width of 1 mm

q (W)	Δx(m)	ΔT_{b-in}(°C)	$\Delta T_{bot-top}$(°C)	$\sigma \Delta x$(m)	$\sigma \Delta T$(°C)	σR_{th}
47	0.0127	5.56	2.31	0.00006	0.28284	0.132
64	0.0127	7.64	3.15	0.00006	0.28284	0.097
88	0.0127	10.20	4.34	0.00006	0.28284	0.071
114	0.0127	13.18	5.61	0.00006	0.28284	0.055
132	0.0127	15.03	6.52	0.00006	0.28284	0.048
186	0.0127	19.15	9.16	0.00006	0.28284	0.035
213	0.0127	20.76	10.46	0.00006	0.28284	0.031
260	0.0127	22.88	12.81	0.00006	0.28284	0.026
305	0.0127	25.05	15.03	0.00006	0.28284	0.022
356	0.0127	27.66	17.52	0.00006	0.28284	0.020
410	0.0127	30.45	20.17	0.00006	0.28284	0.017
450	0.0127	32.20	22.10	0.00006	0.28284	0.016

References

[1] P. Wesling, The heterogeneous integration roadmap: Enabling technology for systems of the future, in: 2020 Pan Pacific Microelectronics Symposium (Pan Pacific), 2020, pp. 1–4, https://doi.org/10.23919/PanPacific48324.2020.9059347.

[2] J.A. Khan, A.K.M.M.M. Morshed, R. Fang, Towards ultra-compact high heat flux microchannel heat sink, Process. Eng. 90 (2014) 11–24, https://doi.org/10.1016/j.proeng.2014.11.798.

[3] S.S. Salvi, A. Jain, A review of recent research on heat transfer in three-dimensional integrated circuits (3-D ICs), IEEE Trans. Compon. Packag. Manuf. Technol. 11 (2021) 802–821, https://doi.org/10.1109/TCPMT.2021.3064030.

[4] Y. Hadad, B. Ramakrishnan, R. Pejman, S. Rangarajan, P.R. Chiarot, A. Pattamatta, B. Sammakia, Three-objective shape optimization and parametric study of a micro-channel heat sink with discrete non-uniform heat flux boundary conditions, Appl. Therm. Eng. 150 (2019) 720–737, https://doi.org/10.1016/j.applthermaleng.2018.12.128.

[5] Y. Hadad, S. Rangararajan, K. Nemati, B. Ramakrishnann, R. Pejman, P.R. Chiarot, B. Sammakia, Performance analysis and shape optimization of a water-cooled impingement micro-channel heat sink including manifolds, Int. J. Therm. Sci. 148 (2020) 106145, https://doi.org/10.1016/j.ijthermalsci.2019.106145.

[6] D. Kisitu, Approximate Compact Thermal-Hydraulic Analytical Models for Laminar Microchannel Impingement Liquid-Cooled Cold Plates for Data Center Thermal Management, M.S.M, Villanova University, 2021 https://www.proquest.com/docview/2618222739/abstract/3DED67357D2F49EEPQ/1 (accessed January 26, 2023).

[7] Y. Hadad, N. Fallahtafti, L. Choobineh, C.H. Hoang, V. Radmard, P.R. Chiarot, B. Sammakia, Performance analysis and shape optimization of an impingement microchannel cold plate, IEEE Trans. Compon. Packag. Manuf. Technol. 10 (2020) 1304–1319, https://doi.org/10.1109/TCPMT.2020.3005824.

[8] D. Kisitu, C. Caceres, M. Zlatinov, D. Schaffarzick, A. Ortega, Experimental investigation of R134a flow boiling in copper foam evaporators for high heat flux electronics cooling, in: American Society of Mechanical Engineers Digital Collection, 2022, https://doi.org/10.1115/IPACK2022-97400.

[9] K. Sefiane, A. Koşar, Prospects of heat transfer approaches to dissipate high heat fluxes: opportunities and challenges, Appl. Therm. Eng. 215 (2022) 118990, https://doi.org/10.1016/j.applthermaleng.2022.118990.

[10] W. Qu, I. Mudawar, Prediction and measurement of incipient boiling heat flux in micro-channel heat sinks, Int. J. Heat Mass Transf. 45 (2002) 3933–3945, https://doi.org/10.1016/S0017-9310(02)00106-0.

[11] I. Mudawar, Two-phase microchannel heat sinks: theory, applications, and limitations, J. Electron. Packag. 133 (2011), https://doi.org/10.1115/1.4005300.

[12] S.T. Kadam, R. Kumar, Twenty first century cooling solution: microchannel heat sinks, Int. J. Therm. Sci. 85 (2014) 73–92, https://doi.org/10.1016/j.ijthermalsci.2014.06.013.

[13] P. Smakulski, S. Pietrowicz, A review of the capabilities of high heat flux removal by porous materials, microchannels and spray cooling techniques, Appl. Therm. Eng. 104 (2016) 636–646, https://doi.org/10.1016/j.applthermaleng.2016.05.096.

[14] D.D. Ma, G.D. Xia, L.X. Zong, Y.T. Jia, Y.X. Tang, R.P. Zhi, Experimental investigation of flow boiling heat transfer performance in zigzag microchannel heat sink for electronic cooling devices, Int. J. Therm. Sci. 145 (2019) 106003, https://doi.org/10.1016/j.ijthermalsci.2019.106003.

[15] T.G. Karayiannis, M.M. Mahmoud, Flow boiling in microchannels: fundamentals and applications, Appl. Therm. Eng. 115 (2017) 1372–1397, https://doi.org/10.1016/j.applthermaleng.2016.08.063.

[16] K.C. Leong, J.Y. Ho, K.K. Wong, A critical review of pool and flow boiling heat transfer of dielectric fluids on enhanced surfaces, Appl. Therm. Eng. 112 (2017) 999–1019, https://doi.org/10.1016/j.applthermaleng.2016.10.138.

[17] C.H. Hoang, G. Mohsenian, N. Fallatafti, V. Radmard, S. Rangarajan, C. Arvin, K. Sikka, S. Schiffres, B. Sammakia, Effects of different coolants on the cooling performance of an impingement microchannel cold plate, in: 2021 37th semiconductor thermal measurement, Modeling & Management Symposium (SEMI-THERM), 2021, pp. 43–49.

[18] S.-M. Kim, I. Mudawar, Thermal design and operational limits of two-phase micro-channel heat sinks, Int. J. Heat Mass Transf. 106 (2017) 861–876, https://doi.org/10.1016/j.ijheatmasstransfer.2016.10.020.

[19] J. Lee, I. Mudawar, Fluid flow and heat transfer characteristics of low temperature two-phase micro-channel heat sinks – part 1: experimental methods and flow visualization results, Int. J. Heat Mass Transf. 51 (2008) 4315–4326, https://doi.org/10.1016/j.ijheatmasstransfer.2008.02.012.

[20] T. Harirchian, S.V. Garimella, Microchannel size effects on local flow boiling heat transfer to a dielectric fluid, Int. J. Heat Mass Transf. 51 (2008) 3724–3735, https://doi.org/10.1016/j.ijheatmasstransfer.2008.03.013.

[21] T. Harirchian, S.V. Garimella, Effects of channel dimension, heat flux, and mass flux on flow boiling regimes in microchannels, Int. J. Multiphase Flow 35 (2009) 349–362, https://doi.org/10.1016/j.ijmultiphaseflow.2009.01.003.

[22] T. Harirchian, S.V. Garimella, The critical role of channel cross-sectional area in microchannel flow boiling heat transfer, Int. J. Multiphase Flow 35 (2009) 904–913, https://doi.org/10.1016/j.ijmultiphaseflow.2009.06.005.

[23] T. Harirchian, S.V. Garimella, A comprehensive flow regime map for microchannel flow boiling with quantitative transition criteria, Int. J. Heat Mass Transf. 53 (2010) 2694–2702, https://doi.org/10.1016/j.ijheatmasstransfer.2010.02.039.

[24] B. Markal, B. Kul, Combined influence of artificial nucleation site and expanding cross section on flow boiling performance of micro pin fins, Int. Commun. Heat Mass Transf. 135 (2022) 106081, https://doi.org/10.1016/j.icheatmasstransfer.2022.106081.

[25] B. Markal, B. Kul, Influence of downstream cross-sectional area ratio on flow boiling characteristics of expanding micro pin fin heat sinks, Int. Commun. Heat Mass Transf. 143 (2023) 106689, https://doi.org/10.1016/j.icheatmasstransfer.2023.106689.

[26] B. Markal, O. Aydin, M. Avci, Effect of aspect ratio on saturated flow boiling in microchannels, Int. J. Heat Mass Transf. 93 (2016) 130–143, https://doi.org/10.1016/j.ijheatmasstransfer.2015.10.024.

[27] A.H. Al-Zaidi, M.M. Mahmoud, T.G. Karayiannis, Effect of aspect ratio on flow boiling characteristics in microchannels, Int. J. Heat Mass Transf. 164 (2021) 120587, https://doi.org/10.1016/j.ijheatmasstransfer.2020.120587.

[28] B.-R. Fu, C.-Y. Lee, C. Pan, The effect of aspect ratio on flow boiling heat transfer of HFE-7100 in a microchannel heat sink, Int. J. Heat Mass Transf. 58 (2013) 53–61, https://doi.org/10.1016/j.ijheatmasstransfer.2012.11.050.

[29] M. Andredaki, K. Vontas, A. Georgoulas, N. Miché, M. Marengo, The effect of channel aspect ratio on flow boiling characteristics within rectangular micro-passages, Int. J. Heat Mass Transf. 183 (2022) 122201, https://doi.org/10.1016/j.ijheatmasstransfer.2021.122201.

[30] P. Cui, Z. Liu, Experimental study on flow boiling in ultrahigh-aspect-ratio copper microchannel heat sink, Appl. Therm. Eng. 223 (2023) 119975, https://doi.org/10.1016/j.applthermaleng.2023.119975.

[31] B. Markal, et al., Experimental investigation of flow boiling in single minichannels with low mass velocities, Int. Commun. Heat Mass Transf. 98 (2018) 22–30, https://doi.org/10.1016/j.icheatmasstransfer.2018.08.002.

[32] K. Balasubramanian, P.S. Lee, C.J. Teo, S.K. Chou, Flow boiling heat transfer and pressure drop in stepped fin microchannels, Int. J. Heat Mass Transf. 67 (2013) 234–252, https://doi.org/10.1016/j.ijheatmasstransfer.2013.08.023.

[33] K. Balasubramanian, P.S. Lee, L.W. Jin, S.K. Chou, C.J. Teo, S. Gao, Experimental investigations of flow boiling heat transfer and pressure drop in straight and expanding microchannels – a comparative study, Int. J. Therm. Sci. 50 (2011) 2413–2421, https://doi.org/10.1016/j.ijthermalsci.2011.07.007.

[34] P. Bai, T. Tang, B. Tang, Enhanced flow boiling in parallel microchannels with metallic porous coating, Appl. Therm. Eng. 58 (2013) 291–297, https://doi.org/10.1016/j.applthermaleng.2013.04.067.

[35] F. Yang, W. Li, X. Dai, C. Li, Flow boiling heat transfer of HFE-7000 in nanowire-coated microchannels, Appl. Therm. Eng. 93 (2016) 260–268, https://doi.org/10.1016/j.applthermaleng.2015.09.097.

[36] D. Deng, W. Wan, Y. Qin, J. Zhang, X. Chu, Flow boiling enhancement of structured microchannels with micro pin fins, Int. J. Heat Mass Transf. 105 (2017) 338–349, https://doi.org/10.1016/j.ijheatmasstransfer.2016.09.086.

[37] J. Chen, S. Zhang, Y. Tang, H. Chen, W. Yuan, J. Zeng, Effect of operational parameters on flow boiling heat transfer performance for porous interconnected microchannel nets, Appl. Therm. Eng. 121 (2017) 443–453, https://doi.org/10.1016/j.applthermaleng.2017.04.115.

[38] D. Lorenzini, Y. Joshi, Numerical modeling and experimental validation of two-phase microfluidic cooling in silicon devices for vertical integration of microelectronics, Int. J. Heat Mass Transf. 138 (2019) 194–207, https://doi.org/10.1016/j.ijheatmasstransfer.2019.04.036.

[39] P.A. Kottke, T.M. Yun, C.E. Green, Y.K. Joshi, A.G. Fedorov, Two-phase convective cooling for ultrahigh power dissipation in microprocessors, J. Heat Transf. 138 (2015), https://doi.org/10.1115/1.4031111.

[40] R. Srikanth, C. Balaji, Experimental investigation on the heat transfer performance of a PCM based pin fin heat sink with discrete heating, Int. J. Therm. Sci. 111 (2017) 188–203, https://doi.org/10.1016/j.ijthermalsci.2016.08.018.

[41] G.K. Marri, R. Srikanth, C. Balaji, Multiple phase change material-based heat sink for cooling of electronics: a combined experimental and numerical study, ASME J. Heat Mass Transf. 145 (2023), https://doi.org/10.1115/1.4056543.

[42] Muhammet Balcilar, A.S. Dalkilic, A. Suriyawong, T. Yiamsawas, S. Wongwises, Investigation of pool boiling of nanofluids using artificial neural networks and correlation development techniques, Int. Commun. Heat Mass Transf. 39 (3) (2012) 424–431.

[43] Mohammad Mahdi Tafarroj, Omid Mahian, Alibakhsh Kasaeian, Kittipong Sakamatapan, Ahmet Selim Dalkilic, Somchai Wongwises, Artificial neural network modeling of nanofluid flow in a microchannel heat sink using experimental data, Int. Commun. Heat Mass Transf. 86 (2017) 25–31.

[44] Yue Qiu, Deepak Garg, Liwei Zhou, Chirag R. Kharangate, Sung-Min Kim, Issam Mudawar, An artificial neural network model to predict mini/micro-channels saturated flow boiling heat transfer coefficient based on universal consolidated data, Int. J. Heat Mass Transf. 149 (2020) 119211.

[45] M.T. Hughes, G. Kini, S. Garimella, Status, challenges, and potential for machine learning in understanding and applying heat transfer phenomena, ASME. J. Heat Transf. 143 (12) (October 18, 2021) 120802, https://doi.org/10.1115/1.4052510. December 2021.

[46] A. Mehralizadeh, S.R. Shabanian, G. Bakeri, Investigation of boiling heat transfer coefficients of different refrigerants for low fin, turbo-B and thermoexcel-E enhanced tubes using computational smart schemes, J. Therm. Anal. Calorim. 141 (3) (2020) 1221–1242, https://doi.org/10.1007/s10973-019-09075-x.

[47] G. Zhu, T. Wen, D. Zhang, Machine learning based approach for the prediction of flow boiling/condensation heat transfer performance in mini channels with serrated fins, Int. J. Heat Mass Transf. 166 (2021) 120783, https://doi.org/10.1016/j.ijheatmasstransfer.2020.120783.

[48] H.M. Park, J.H. Lee, K.D. Kim, Wall temperature prediction at critical heat flux using a machine learning model, Ann. Nucl. Energy 141 (2020) 107334, https://doi.org/10.1016/j.anucene.2020.107334.

[49] N. Fallahtafti, S. Rangarajan, Y. Hadad, C. Arvin, K. Sikka, C.H. Hoang, G. Mohsenian, V. Radmard, S. Schiffres, B. Sammakia, Shape optimization of hotspot targeted micro pin fins for heterogeneous integration applications, Int. J. Heat Mass Transf. 192 (2022) 122897, https://doi.org/10.1016/j.ijheatmasstransfer.2022.122897.

[50] C.H. Hoang, S. Rangarajan, S. Khalili, B. Ramakrisnan, V. Radmard, Y. Hadad, S. Schiffres, B. Sammakia, Hybrid microchannel/multi-jet two-phase heat sink: a benchmark and geometry optimization study of commercial product, Int. J. Heat Mass Transf. 169 (2021) 120920, https://doi.org/10.1016/j.ijheatmasstransfer.2021.120920.

[51] C.H. Hoang, N. Fallahtafti, S. Rangarajan, A. Gharaibeh, Y. Hadad, C. Arvin, K. Sikka, S.N. Schiffres, B. Sammakia, Impact of fin geometry and surface roughness on performance of an impingement two-phase cooling heat sink, Appl. Therm. Eng. 198 (2021) 117453, https://doi.org/10.1016/j.applthermaleng.2021.117453.

[52] N. Fallahtafti, C.H. Hoang, Y. Hadad, S. Rangarajan, S. Schiffres, B. Sammakia, Design improvement of a commercial impingement two-phase cold plate used for high heat flux applications, in: 2022 38th Semiconductor Thermal Measurement, Modeling & Management Symposium (SEMI-THERM), 2022, pp. 30–35.

[53] V. Semin, M. Bardsley, O. Rosten, C. Aldham, Application of a multilevel unstructured staggered solver to thermal electronic simulations, in: 2015 31st Thermal Measurement, Modeling Management Symposium (SEMI-THERM), 2015, pp. 287–292, https://doi.org/10.1109/SEMI-THERM.2015.7100174.

[54] R.J. Moffat, Describing the uncertainties in experimental results, Exp. Thermal Fluid Sci. 1 (1988) 3–17, https://doi.org/10.1016/0894-1777(88)90043-X.

[55] M.S. El-Genk, M. Pourghasemi, Experimental investigation of saturation boiling of HFE-7000 dielectric liquid on rough copper surfaces, Thermal Sci. Eng. Prog. 15 (2020) 100428, https://doi.org/10.1016/j.tsep.2019.100428.

[56] S. Mukherjee, I. Mudawar, Pumpless loop for Narrow Channel and Micro-Channel boiling, J. Electron. Packag. 125 (2003) 431–441, https://doi.org/10.1115/1.1602708.

[57] R.A. Buchanan, T.A. Shedd, Extensive parametric study of heat transfer to arrays of oblique impinging jets with phase change, J. Heat Transf. 135 (2013), https://doi.org/10.1115/1.4024625.

[58] C.H. Hoang, S. Khalili, B. Ramakrisnan, S. Rangarajan, Y. Hadad, V. Radmard, K. Sikka, S. Schiffres, B. Sammakia, An experimental apparatus for two-phase cooling of high heat flux application using an impinging cold plate and dielectric coolant, in: 2020 36th Semiconductor Thermal Measurement, Modeling & Management Symposium (SEMI-THERM), 2020, pp. 32–38, https://doi.org/10.23919/SEMI-THERM50369.2020.9142831.

[59] T. Dormer Jr., A.E. Bergles, Pressure drop with surface boiling in small-diameter tubes, in: DSR Report 8767–31, Massachusetts Institute of Technology, Cambridge, MA, 1964.

[60] Y. Qiu, D. Garg, L. Zhou, C.R. Kharangate, S.-M. Kim, I. Mudawar, An artificial neural network model to predict mini/micro-channels saturated flow boiling heat transfer coefficient based on universal consolidated data, Int. J. Heat Mass Transf. 149 (2020) 119211, https://doi.org/10.1016/j.ijheatmasstransfer.2019.119211.

[61] S.-M. Kim, I. Mudawar, Universal approach to predicting saturated flow boiling heat transfer in mini/micro-channels – Part II. Two-phase heat transfer coefficient, Int. J. Heat Mass Transf. 64 (2013) 1239–1256, https://doi.org/10.1016/j.ijheatmasstransfer.2013.04.014.

[62] S. Rangarajan, Y. Hadad, L. Choobineh, B. Sammakia, Minimizing temperature nonuniformity by optimal arrangement of hotspots in vertically stacked three-dimensional integrated circuits, J. Electron. Packag. 142 (2020), https://doi.org/10.1115/1.4047471.

[63] K. Deb, A. Pratap, S. Agarwal, T. Meyarivan, A fast and elitist multiobjective genetic algorithm: NSGA-II, IEEE Trans. Evol. Comput. 6 (2002) 182–197, https://doi.org/10.1109/4235.996017.